

Chandra LETGS spectroscopy of the Quasar MR 2251–178 and its warm absorber

J.M. Ramírez, Stefanie Komossa, Vadim Burwitz

Max-Planck-Institut für extraterrestrische Physik, D-85741 Garching, Germany

and

Smita Mathur

Department of Astronomy, Ohio State University, 140 West 18th Avenue, Columbus, OH 43204

ABSTRACT

We present an analysis of our *Chandra* Low Energy Transmission Grating Spectrometer (LETGS) observation of the quasar MR 2251–178. The warm absorber of MR 2251–178 is well described by a hydrogen column density, $N_{\text{H}} \approx 2 \times 10^{21} \text{ cm}^{-2}$, and an ionization parameter $\log(\xi) \approx 0.6$. We find in the spectrum weak evidence for narrow absorption lines from Carbon and Nitrogen which indicate that the ionized material is in outflow. We note changes (in time) of the absorption structure in the band (0.6 – 1) keV (around the UTAs plus the O VII and O VIII K-edges) at different periods of the observation. We measure a (0.1 – 2) keV flux of $2.58 \times 10^{-11} \text{ ergs cm}^{-2} \text{ s}^{-1}$. This flux implies that the nuclear source of MR 2251–178 is in a relatively low state. No significant variability is seen in the light curve. We do not find evidence for an extra cold material in the line of sight, and set an upper limit of $N_{\text{H}} \approx 1.2 \times 10^{20} \text{ cm}^{-2}$. The X-ray spectrum does not appear to show evidence for dusty material, though an upper limit in the neutral carbon and oxygen column densities can only be set to $N_{\text{C I}} \approx 2 \times 10^{19} \text{ cm}^{-2}$ and $N_{\text{O I}} \approx 9 \times 10^{19} \text{ cm}^{-2}$, respectively.

Subject headings: galaxies: active – X-rays: galaxies – quasars: individual (MR 2251–178)

1. Introduction

Warm absorbers have provided deep insights into the nuclear environment of Active Galaxies (AGNs). Halpern (1984) reported its presence for the first time using the *Einstein*

observation of the QSO MR 2251–178. Since then, warm absorbers have been commonly found in about 50 % of the AGN spectra (see Komossa & Hasinger 2003; Crenshaw et al. 2003, for reviews), and their study has enriched our knowledge about the ionization and the kinematics of the gas composing these systems, important for the understanding of the evolution of these objects, and the AGN unification picture.

In this context MR 2251–178, at $z = 0.06398$ (Bergeron et al. 1983), has been the subject of various studies, first due to its historical importance as the first quasar discovered by X-ray observations (Ricker et al. 1978), the first warm absorber reported (Halpern 1984), and because it displays a number of outstanding characteristics. It is surrounded by a large [O III] emission line region, located in the outskirts of a cluster of galaxies (Bergeron et al. 1983), with a high ratio L_x/L_{opt} . Several studies have been focused on the characterization of the absorbing material properties. Komossa (2001) fitted a warm absorber model to the *ROSAT* observation of MR 2251–178, and found a high ionization state of the absorber ($\log U \sim 0.5$), and a column density of $N_H \sim 10^{22.6} \text{ cm}^{-2}$. Monier et al. (2001) reported the presence of absorption lines of N v $\lambda 1240$ and C IV $\lambda 1549$ blueshifted by few hundreds of km s^{-1} . Ganguly et al. (2001) noticed variability of the C IV $\lambda 1549$ line by taking observations from the *Hubble Space Telescope* (HST) 4 years apart, and inferred a maximum distance from the source of ~ 2.4 kpc.

More recently, Kaspi et al. (2004) established a scenario where clouds crossing our line of sight show up by the presence of absorption lines coming from high ionization states, displaying a wide velocity range from 0 to $\sim 600 \text{ km s}^{-1}$, taking a 8.5 yr set of data from *ASCA*, *BeppoSAX* and *XMM-Newton*.

Gibson et al. (2005) analyzed data from the *High Energy Transmission Grating* on board *Chandra*, and found evidence in the spectrum of MR 2251–178 of highly ionized, high-velocity ($v \sim 12,000 - 17,000 \text{ km s}^{-1}$) outflowing material. They report similar column densities to those of Kaspi et al. (2004), of a few 10^{21} cm^{-2} , and establish conditions for the accretion and mass-loss rates.

From the Fe XXVI L_α line, Gibson et al. (2005) concluded that, unless the absorber covering factor is very low, the mass-loss rate is approximately an order of magnitude higher than the accretion rate that would provide the radiation power of MR 2251–178 ($\sim 0.2 M_\odot \text{ yr}^{-1}$, at 10 % efficiency). This is a different conclusion from that reached by Monier et al. (2001), in the *Hubble Space Telescope* (HST) analysis of the same object, where they established that the accretion and mass-loss rates are essentially the same. The inquiry into this point is of relevance to the understanding of the evolution mechanisms in the nucleus of MR 2251–178. On the other hand, the HETGS high resolution observation also reveals the presence of emission lines coming from highly-ionized species, and shows that the emitting material is

not in our line of sight, opening the possibility that the absorption and the emission lines have different physical origins or that they are located at different distances from the nucleus. This phenomenon has been observed in NGC 4051 in the optical/ultraviolet band. Komossa & Fink (1997) concluded that the coronal emission lines from lowly ionized species of Fe ([Fe VII]-[Fe XI]) observed in the spectrum of this object, have a *different physical origin* from the warm absorber, consistent with the fact that they could come from a different spatial region, the warm absorber located at the nucleus and the coronal lines extended out of ~ 150 pc (Nagao et al. 2000).

Finally dusty warm absorbers have been found in a number of AGN (Komossa & Hasinger 2003, and references therein for a review) and are predicted to leave their mark on the X-ray spectra of AGN, for instances the K-edges of O I and C I (Komossa & Fink 1997; Komossa & Bade 1998), and the Fe-L edge (Lee et al. 2001). For the first time, we search for the presence of a dusty warm absorber in MR 2251–178. Based on ROSAT data, Komossa (2001) speculated about the presence of a second dusty warm absorber in MR 2251–178, this second warm absorber dusty, but the data did not allow multi-component fitting, which would provide important implications on the global structure of MR 2251–178.

It is clear from this introduction that each of the previous missions and the use of more powerful spectroscopic instruments lead to new perspectives regarding the properties and the evolution of the nuclear environment of MR 2251–178. We present an overview and an analysis of the spectrum of MR 2251–178 as it is seen with the *Low Energy Transmission Grating Spectrometer* (LETGS) on board *Chandra*. The spectral resolution power of the instrument allows us to confirm some of the previous conclusions about the ionization and the kinematics of the warm absorber of MR 2251–178, and shed new light on the evolution, ionization and composition of this system.

Technical details on the observation and data reduction are given in §2. Our spectral analysis is given in §3.2. The mean properties of the warm absorber of MR 2251–178 are presented in §3.4, with the corresponding spectral absorption lines analysis. To finish, we made a temporal analysis on the absorption structure around the O VII and O VIII K-edges in §4. We discuss the results in §5 and conclude in §6. Throughout this paper, we use the following cosmological parameters: $H_0 = 70 \text{ km s}^{-1} \text{ Mpc}^{-1}$, $\Omega_M = 0.3$ and $\Omega_\lambda = 0.7$.

2. Observation and Data Reduction

We obtained a ~ 80 ks exposure time observation of MR 2251–178, performed with the *Low Energy Transmission Grating Spectrometer* (LETGS, Brinkman et al. 2000) on board

Chandra (under the sequence number 700405 and OBS ID 02966). A log of the observation is presented in Table 1. The spectrum was obtained by reducing the data with the Chandra Interactive Analysis of Observation (CIAO¹) version 3.3.

We use the default spectral extraction region (i.e., a “bow-tie” shaped region). When the LETG (*Low Energy Transmission Grating*) is used with the HRC-S detector (*High Resolution Camera*), this comprises a central rectangle abutted to outer regions whose widths increase as the dispersion distance increases. The background region is taken from above and below the dispersed spectra. The region shape for both, source and background negative and positive orders is precisely given in the file `letgD1999-07-22regN0002.fits`, that can be found at the LETGS calibration webpage ².

Having properly extracted both, source and background spectra from each arm, we merged them, obtaining added source and background spectra. This is intended to increase the signal-to-noise ratio (S/N) of the final spectrum, and the spectral analysis (throughout this work) is based on this co-added spectrum. The effective areas (EA) for orders from 2 to 10 used in fitting procedures were taken from the LETG+HRC-S effective areas webpage ². For the first order we used the corrected EA of Beuermann et al. (2006). EA orders from 1 to 10 (positive and negative orders) were summed to be used with the corresponding co-added spectrum.

The nominal LETGS wavelength range is $1.24 - 175 \text{ \AA}$ ($0.07 - 10 \text{ keV}$). However, we restrict our spectral analysis to the range $1.24 - 124 \text{ \AA}$ ($\sim 0.1 - 10 \text{ keV}$). In the range $\sim 0.07 - 0.09 \text{ keV}$ the S/N ratio is low (≈ 1.4 at $\sim 0.09 \text{ keV}$), and we exclude bins in this band from our analysis. Also, we exclude bins that fall in the bands where the gaps of the detector (HRC-S) are located (i.e., $52 - 56 \text{ \AA}$ and $62 - 66 \text{ \AA}$, for left and right gaps respectively). Figure 1 shows the summed (positive and negative dispersion orders) background subtracted count rate spectrum of MR 2251–178 adaptively binned to have at least 100 counts from the source per bin over the range considered in this work. It is known that an instrumental feature $\sim 2.08 \text{ keV}$, related to the mirror, could be modeled by an edge with negative optical depth ³. We model this Ir M edge of the mirror by using an edge model with energy fixed to 2.08 keV , and an optical depth equal to -0.15 . So all our fits include this negative edge model. All wavelengths and energies are presented in the observed frame.

¹<http://cxc.harvard.edu/ciao>

²<http://cxc.harvard.edu/cal/Letg>

³http://cxc.harvard.edu/ccw/proceedings/03_proc/presentations/marshall12/s001.html

2.1. Source Extent and Light Curve

In order to search for evidence of a spatial extent of the source or the presence of other possible X-ray sources, for example jets, close to MR 2251–178, we take the zero-order image (Chip 2 on the HRC-S) of MR 2251–178 centered at RA= 22:54:05.08 and Dec(J2000)= -17°34′55″ in a field of view of 10″ × 10″. The extent of the emission (and the 90 % encircled energy; computed with the `celldetect` command of CIAO⁴) is consistent with being inside the point-spread function (PSF) dominated zone (for the LETGS $\sim 1.8''$). We conclude that no evidence of appreciable extent of the source is found in this observation (we also checked for angular dependence in the X-ray image, and found that the emission of the object is symmetrically distributed).

The light curve constructed from the zero-order of the observation is shown in Figure 2 (top panel). Counts are binned to 200 s bins. We find a mean value of 111 counts bin⁻¹ (horizontal red line) without any significant variation within 1σ (horizontal green lines). In the bottom panel we present the light curve of the background (see definition below), which shows that strong count variations occur in several time intervals. Data from these intervals were excluded from the spectral analysis presented below. We removed data coming from time intervals whose count rate were above 3σ (horizontal green lines) from the mean value (horizontal red line). The final spectrum was constructed from these good time intervals (GTI), time intervals where counts are within 3σ from the mean value of the fluctuation exhibited by the background. A circular region around the zero-order image with a radius of 10″ was used to extract the source light curve. The background extraction region is defined by four circles with radii of 25″ equidistantly distributed from the source in order to avoid contamination from events associated with dispersion and cross-dispersion directions.

3. Global Spectral Models

3.1. Flux and Luminosity (0.1 – 10 keV)

To compute the hard, and soft X-ray fluxes we fit a simple power-law to the total spectrum⁵ absorbed only by the Galactic column density of $N_{\text{H}} = 2.77 \times 10^{20} \text{ cm}^{-2}$ (Lockman & Savage

⁴http://cxc.harvard.edu/ciao3.3/download/doc/detect_manual/cell_run.html

⁵The added spectrum described in section 2 adaptively binned to have at least 100 counts from the source per bin. The fit was carried out in XSPEC 11, and the fluxes and luminosities computed with the commands `flux` and `lumin` respectively (the used band was 0.1 – 10 keV, and the model includes the Ir edge at 2.08 keV with $\tau = -0.15$). We note that the LETGS spectrum of MR 2251–178 is dominated by the soft X-rays

1995), and we obtain a photon index of $\Gamma_x = 1.94_{-0.03}^{+0.03}$ and a normalization value of $5.64_{-0.08}^{+0.08} \times 10^{-3}$ photons $\text{keV}^{-1} \text{cm}^{-2} \text{s}^{-1}$ at 1 keV. Then we integrate the unabsorbed power-law⁶ to obtain a flux in the 0.1 – 2 keV band $f_{(0.1-2 \text{ keV})} = 2.58_{-0.03}^{+0.04} \times 10^{-11}$ ergs $\text{cm}^{-2} \text{s}^{-1}$, and the (0.1 – 2) keV luminosity is $L_{(0.1-2 \text{ keV})} = 2.54 \times 10^{44}$ erg s^{-1} , a factor of ≈ 1.5 fainter than the ROSAT soft X-ray observation. The (2 – 10) keV flux is $f_{(2-10 \text{ keV})} = 1.64_{-0.05}^{+0.05} \times 10^{-11}$ ergs $\text{cm}^{-2} \text{s}^{-1}$, and a (2 – 10) keV source luminosity $L_{(2-10 \text{ keV})} = 1.62 \times 10^{44}$ erg s^{-1} . This is ≈ 30 % lower than the 2 – 10 keV luminosity measured by Gibson et al. (2005) of $L_{(2-10 \text{ keV})} = 2.41 \times 10^{44}$ erg s^{-1} (but see footnote 5). In our computation, 284 of the total of 321 bins included in this analysis are in the 0.1 – 2 keV band, so all the spectral analysis is actually driven by the *soft* part of the spectrum. The information contained in the 0.1 – 0.5 keV band is important to conclude that the soft X-ray flux is between ~ 10 – 80 % of the hard fluxes historically measured from the spectrum of MR 2251–178. Recently, this object has been observed in the hard X-ray band (14–195 keV) with the *Swift* Burst Alert Telescope (BAT), with a $L_{(14-195 \text{ keV})} = 10^{45}$ erg s^{-1} (Markwardt et al. 2005). Taking our best-fit power-law and integrating over the 14–195 keV band, we predict a luminosity $L_{(14-195 \text{ keV})} = 3 \times 10^{44}$ erg s^{-1} , a few factor lower than the *Swift* observation. The full range (0.1 – 10 keV) luminosity, is $L_{(0.1-10 \text{ keV})} = 4.17 \times 10^{44}$ erg s^{-1} . Our measured (0.1 – 2) keV flux allows us to conclude that MR 2251–178 is in a relatively low soft X-ray state.

3.2. Spectral Models

The rest of the spectral analysis of the present work was carried out with the Interactive Spectral Interpretation System package⁷ (ISIS ver. 1.4.4) using the XSPEC modules from the LHEASOFT libraries⁸.

MR 2251–178 is surrounded by a giant emission-line nebula of ~ 10 – 200 kpc extent (e.g., Bergeron et al. 1983; Macchetto et al. 1990). Bergeron et al. (1983) estimated a column density of a few times 10^{21}cm^{-2} of the emission-line gas. They speculated about the presence of an extended neutral H I halo around MR 2251–178 which should be detectable in H I 21cm observations, or in the soft X-ray band, if also located along our line-of-sight

band (i.e., < 2 keV). So there might be an underestimate of the flux in the band 2 – 10 keV. The error can be estimated around 20 %.

⁶We also compute the flux using a two powerlaws model, which represents in a better way the 2 – 10 keV band, with deviations from the data not larger than 10%. The resulted fluxes do not change significantly.

⁷<http://space.mit.edu/CXC/ISIS/index.html>

⁸<http://heasarc.nasa.gov/docs/software/lheasoft/>

(see also Sect 6.1 of Komossa 2001, for further motivation). We begin our fitting procedure by searching for, and placing constraints on, any cold material along our line-of-sight to the quasar which is in excess to the Galactic absorption toward MR 2251–178.

We fit a simple power-law, absorbed by a column of cold gas in the line of sight, to the X-ray spectrum of MR 2251–178. Both, the power-law parameters and the column density are free parameters. The best-fit photon index and column density we obtain are $\Gamma_x = 1.79_{-0.02}^{+0.02}$ and $N_H = 1.68_{-0.07}^{+0.07} \times 10^{20} \text{ cm}^{-2}$, respectively. We plot in Figure 3 the best-fit absorbed power-law model along with the spectrum of MR 2251–178 in energy space. The best-fit column density is about 40 % lower than the Galactic value toward MR 2251–178 ($2.77 \times 10^{20} \text{ cm}^{-2}$, Lockman & Savage 1995). If we fix the column density to the Galactic value and re-fit, we obtain a slight change in the value of the photon index to $\Gamma_x \sim 1.9$ and the fit gets worse with a change in $\Delta\chi^2 \sim 140$. Taking the upper limit of the extra cold material reported by Komossa (2001) of $\Delta N_H \equiv 5 \times 10^{19} \text{ cm}^{-2}$ and including it in the column of gas, we obtain a photon index slightly steeper and the fit gets worse if we increase the column density of the extra cold material by one and two times ΔN_H (see rows 3 and 4 in Table 2), increasing χ^2 (respect with N_H free to vary) by $\Delta\chi^2 = 260$ and 396 respectively.

We also carefully investigate if excess X-ray absorption, above the Galactic value, and a blackbody component could be combined to compensate each other so as to mimic a less absorbed spectrum. This case is shown graphically in Figure 3 in solid for the composite model (i.e., `zphabs × [pl+bb]`⁹) in comparison with the absorbed power-law (top panel). The best-fit intrinsic (AGN frame) extra column density has a value (given the data) consistent with zero.

We tried a last model composed of two power-laws and cold absorption. The result is shown in Figure 3 (second panel from top to bottom). A steep power-law ($\Gamma_x \approx 3.5$), with help of the cold absorption, describes relatively well the soft band of the spectrum ($\sim 0.1 - 0.6 \text{ keV}$). A flatter second power-law with $\Gamma_x \sim 1$ is responsible for describing the hard band ($\sim 0.7 - 10 \text{ keV}$). An extra absorption, above the Galactic value, arises naturally from the fit (with the same number of parameters as the `pl+bb` model). A material with column density $N_H \approx 1.2 \times 10^{20} \text{ cm}^{-2}$ accounts for this extra absorption (see the best-fit column density in Table 2 row 6). We enforced this model to have an excess absorption of this best-fit column density plus 1 and 2 times ΔN_H , and re-fit, obtaining worse fits (see rows 7 and 8 in Table 2). We conclude that there is little evidence for cold excess absorption with a column density of $N_H \sim 10^{21} \text{ cm}^{-2}$. The maximum amount of cold absorption we can hide

⁹power-law plus blackbody modified by a column of gas in the AGN-frame. The model is corrected by the Galactic absorption.

in the X-ray spectrum of MR 2251–178, based on the model fit involving two powerlaws, is $N_{\text{H}} \approx 1.2 \times 10^{20} \text{ cm}^{-2}$, and we consider this as a safe upper limit to the excess absorption along the line of sight at the epoch of observation.

From now on, all the models considered in this study are multiplied by an absorption column of gas (**phabs** model in XSPEC¹⁰) with $N_{\text{H}} = 2.77 \times 10^{20} \text{ cm}^{-2}$ to describe the Galactic absorption toward MR 2251–178 (Lockman & Savage 1995). First, we focus our attention on the fit of a power-law to describe the 1.24–124 Å band of the spectrum. A single power-law gives $\Gamma_{\text{x}} = 1.94_{-0.02}^{+0.02}$, with large residuals (i.e., 15–40 %) in the ~ 1.2 –7 Å and close to 18 Å (see Figure 4), and a poor statistical fit quality of $\chi_{\nu}^2 = 3.00$. We included a thermal component to account for any soft X-ray excess. A blackbody with a temperature of $kT = 81.5_{-2.0}^{+2.0}$ eV significantly improved the fit with $\chi_{\nu}^2 = 1.63$ (for d.o.f = 305). With this addition, the slope of the power-law changes to a flatter value of $\Gamma_{\text{x}} = 1.53_{-0.02}^{+0.02}$, and the model agrees with the data within 30 % almost from ~ 1.2 to 40 Å, except for the residual around 18 Å.

Now, let us consider the absorption features at ≈ 18 Å and ≈ 15 Å in turn. Komossa (2001) fitted a power-law with two edges at the theoretical positions of O VII and O VIII, 739 eV and 871 eV respectively, representing the warm absorber, obtaining $\tau_{\text{O VII}} = 0.22 \pm 0.11$ and $\tau_{\text{O VIII}} = 0.24 \pm 0.12$. The high sensitivity and resolution of the *Chandra* LETG spectrometer coupled with the good quality of the observation of MR 2251–178, allow us to fit these features with a high precision. Our **p1 × 2 edges** (≈ 18 Å and ≈ 15 Å in the observed frame) model gives us a significant improvement ($\chi_{\nu}^2 = 1.38$ for 305 d.o.f) over the fit of the power-law alone ($\chi_{\nu}^2 = 3.00$ for 307 d.o.f) and the power-law plus the blackbody component as well ($\chi_{\nu}^2 = 1.63$ for 305 d.o.f). This model is in agreement with the data $\approx \pm 15$ % (data/model $\approx 1.00 \pm 0.15$, Figure 4) over almost the entire spectrum, except for the wavelength range 1.2–6 Å (and possibly at wavelengths $\gtrsim 60$ Å, but see the large errors). The continuum optical depths are $\tau_{\text{O VII}} = 0.56_{-0.04}^{+0.05}$ and $\tau_{\text{O VIII}} = 0.22_{-0.04}^{+0.05}$. We compare these values with those obtained from *ROSAT*. In the case of O VIII they appear to agree within the error bars. However, in the case of O VII the optical depth is approximately a factor of 2.5 higher. In this direct comparison model-to-model, the *Chandra* data suggests that the contribution of this feature has changed over the years (\sim fifteen).

Finally, we can build a model combining all the ingredients mentioned above leading us to a global view of the spectrum: A power-law plus a soft-thermal component modified by two warm absorber edges. This model is shown in Figure 4 and the maximum deviation of

¹⁰<http://heasarc.nasa.gov/docs/xanadu/xspec/manual-> The abundances are solar from Anders & Grevesse (1989)

the ratio data/model is $\pm 15\%$ over almost the entire spectrum, with $\chi^2_\nu = 1.25$ (for 303 d.o.f). The F-test identifies this improvement (the inclusion of the black body emission) as significant (at $> 99\%$ significance level), over the `p1 × 2 edges` model. The blackbody has a temperature of $kT \sim 50$ eV with the slope of the power-law being in agreement with other models of this study ($\sim 1.7 - 2$) and with slopes reported by previous missions (i.e. *ROSAT*), but not with the flatter slope of ~ 1.4 reported recently by Gibson et al. (2005) in the HETGS observation of the same object. We can see that the inclusion of the strong O VII feature displaces the temperature of the blackbody from $kT \sim 80$ to 50 eV with respect to the `p1+bb` without edges. The reduced temperature of the `bb` helps to improve the fit in the range ~ 20 to 60 Å, giving an improvement of $\Delta\chi^2 \approx 110$. The model parameters are quoted in Table 3. The four models are plotted in Figure 4 upon the background subtracted count rate spectrum of MR 2251–178 in the wavelength space (re-binned to have at least 100 counts from the source per bin).

3.3. A Dusty Warm Absorber?

Dusty warm absorbers have been found to imprint their hallmark on the X-ray spectra of several AGN (e.g. Komossa & Fink 1997; Komossa & Bade 1998; Lee et al. 2001). We investigate the possibility of the presence of a dusty warm absorber by looking at the position of two important edges, predicted to be strong and noticeable in the X-ray band; the neutral carbon edge at 291 eV (from the graphite species), and the O I edge at 538 eV (from silicates). Figure 5 shows the position of these two edges (the edges corresponding to the H- and He-like oxygen features are included in the model but they lie off the figure axis), in the observer’s frame (also marked is the Galactic neutral oxygen as O I_{gal}). These edges are not clearly seen in the spectrum, but this does not preclude their potential addition and improvement to the model in the fitting. In Table 4 we present the result of fitting the spectrum of MR 2251–178 with a model that is composed of a Galactic absorbed power-law modified by four edges, the K-edges of C I, O I, O VII and O VIII. In order to search for fine features, we used a larger number of bins in the fit, 50 counts from the source per bin. In terms of goodness of the fit, this is equal to the `p1 × 2 edges` model, with $\chi^2_\nu = 1.22$ (for 587 d.o.f). However, letting the four edges vary freely, the C I optical depths has no lower limits. An upper limit can be set on the dusty material if it exists. We have enforced the $\tau_{\text{C I}}$ to be equal to 0.08 (the upper limit of this measurement), letting all the other optical depths free to vary, and re-fit. We set this as an upper limit on the $\tau_{\text{C I}}$ parameter, since the fit does not get worse with respect to the previous one (see row 2 in Table 4). This translates in a C I column density $N_{\text{C I}} \approx 2 \times 10^{19} \text{ cm}^{-2}$. Doing the same with the $\tau_{\text{O I}}$ (taking the upper limit of the best-fit), we obtain no significant change with respect to the best-fit χ^2 (see row 3),

and we consider $\tau_{\text{O I}} = 0.09$ as the upper limit on $\tau_{\text{O I}}$, which translates in $N_{\text{O I}} \approx 9 \times 10^{19} \text{ cm}^{-2}$ (we used the photoionization cross sections from Morrison & McCammon 1983, at their respective energies). For typical Galactic gas/dust ratios, our observed upper limit is not sensitive enough to provide significant constraints on the dust in MR 2251–178.

3.4. Mean Warm Absorber

In this section we discuss the global view of the spectrum of MR 2251–178, in terms of a more physical model. Visually, the strongest spectral feature is the broad absorption structure around 17 Å (see Figure 6), recognized as the hallmark of the warm absorber (e.g., George et al. 1998). Detailed calculations have demonstrated that this structure is made (mainly) by the O VII-K edge and by the Fe M-shell $2p-3d$ unresolved transition array (UTA) between 16–17 Å (Behar et al. 2001). The ionization condition under this structure is strong enough to dominate the emergent spectrum, have been the subject of several theoretical and observational works (e.g., Krongold et al. 2003; Gu et al. 2006), due to in part, the particular sensitivity of this feature to the ionization state of the gas responsible for the absorption.

To describe the state of the gas, we build a grid of photoionization models assuming ionization and thermal equilibrium. Under conditions of ionization equilibrium the state of the gas depends mostly (apart from n_{H} , abundances and column density) upon the shape of the ionizing spectrum and the ionization parameter ξ , that we define as in Tarter et al. (1969):

$$\xi = \frac{4\pi F_{\text{ion}}}{n_{\text{H}}}, \quad (1)$$

where F_{ion} is the total ionizing flux ($F_{\text{ion}} = L_{\text{ion}}/[4\pi r^2]$, see below for definition of L_{ion}), and n_{H} is the gas density. We have carried out all the photoionization calculations using the XSTAR¹¹ code with the atomic data of Bautista & Kallman (2001). The code includes all the relevant atomic processes (including inner shell processes) and computes the emissivities and optical depths of the most prominent X-ray and UV lines identified in AGN spectra. Our models are based on spherical shells illuminated by a point-like X-ray continuum source. The input parameters are the source spectrum, the gas composition, the gas density n_{H} , the column density and the ionization parameter. The source spectrum is described by the

¹¹Version 2.1kn6. UTAs included. However, this version does not include the corrections (for some atomic line transitions) given by Gu et al. (2006). We have re-computed our models based on an updated version of XSTAR (kindly provided by T. Kallman) which does include the corrections of Gu et al. (2006). We find that the change in the outflow velocity is only $\sim 1\%$. Part of the reason is that the LETGS has a spectral resolution of $\approx 50 \text{ mÅ}$, while the changes reported by Gu et al. (2006) were $\approx 15 - 45 \text{ mÅ}$.

spectral luminosity $L_\epsilon = L_{\text{ion}}f_\epsilon$, where L_{ion} is the integrated luminosity from 1 to 1000 Ryd, and $\int_1^{1000 \text{ Ryd}} f_\epsilon d\epsilon = 1$. The spectral function is taken to be the ionizing spectrum of Leighly (2004). The gas consists of the following elements, H, He, C, N, O, Ne, Mg, Si, S, Ar, Ca and Fe. We use the abundances of Grevesse et al. (1996) in all our models (we use the term *solar* for these abundances). We adopt a turbulent velocity of 100 km s^{-1} , and a gas density $n_{\text{H}} = 10^8 \text{ cm}^{-3}$.

3.4.1. Global Absorption

We have fit the X-ray spectrum of MR 2251–178 with our XSTAR based photoionization models. First of all, we find that independent of column density, a relatively low ionization parameter is needed; else, the spectrum in the Fe UTA band is not well reproduced. We demonstrate this point in Figure 6. It shows the resulting absorption spectrum for several ionization states. For illustrative purposes, here we fix $N_{\text{H}} = 4 \times 10^{21} \text{ cm}^{-2}$. In the top panel we can see the spectrum resulting at high ionization parameter, $\log(\xi) = 1.5$ and 2. The bottom panel shows the spectrum at lower ionization states with $\log(\xi) = 0.5, 0.7$ and 0.9 , in black, red and dark blue respectively. From this we can rule out high ionization states alone to describe this band (though Kaspi et al. 2004, reported the use of a multi-component model to represent the spectrum of MR 2251–178, we were not able to find a significant improvement on the fit over the one-absorber component), because these models always give large residuals in the UTA band (see below).

Nevertheless, for our best-fit, single component photoionization model (`p1` \times `xstar_model` \equiv X_1 , Figure 7), we obtain the following parameters: a column density of $N_{\text{H}} = 4.77_{-0.29}^{+0.31} \times 10^{21} \text{ cm}^{-2}$, an ionization parameter $\log(\xi) = 1.83_{-0.06}^{+0.06}$ and a photon index $\Gamma_{\text{x}} = 1.96_{-0.02}^{+0.02}$. While the fit well describes the long wavelength part of the absorption feature (with respect to the centroid around $\sim 17.4 \text{ \AA}$), there exists a large residual in the shorter wavelength range ($\gtrsim 50 \%$), resulting in a fit with $\chi_\nu^2 = 1.54$ (for 587 d.o.f). Motivated by the good result of including a thermal component to describe any soft excess, and also by the fact that the X-ray spectrum of this object has been fitted before including a thermal component (for example in Gibson et al. 2005), we include in our model a blackbody, characterized by its temperature kT (i.e., `p1+bb` \times `xstar_model` \equiv X_2). The inclusion of the blackbody improved the fit, which gives $\chi_\nu^2 = 1.27$ (and d.o.f = 585). But we went further, and inspected the possibility that the absorbing gas in MR 2251–178 is flowing outward from the center of the system with velocities $\sim 0 - 2000 \text{ km s}^{-1}$. For that purpose we shift the modeled spectrum (the absorber) by a grid of velocities keeping fixed the outflow velocity and letting the others parameters of interest free to vary. For X_1 we found that it favors an outflow

velocity $\approx 200 \text{ km s}^{-1}$. In the case of X_2 , the model points to an outflow velocity $\approx 1200 \text{ km s}^{-1}$. After finding statistically motivated outflow velocities for our models we were able of thawing them and find the best-fit outflow velocity.

The $xstar_{\text{model}}$ plus the blackbody (X_4) gives a $\chi^2_\nu = 1.22$ (with d.o.f = 584), and the following best-fit parameters: $N_{\text{H}} = 2.25^{+0.28}_{-0.25} \times 10^{21} \text{ cm}^{-2}$, $\log(\xi) = 0.63^{+0.06}_{-0.06}$, $kT = 89.5^{+2.5}_{-2.5} \text{ eV}$, and $v_{\text{out}} = -1100^{+60}_{-210} \text{ km s}^{-1}$. An inspection of Figure 7 reveals a good agreement between the data and the model, and the removal of the residual around $\sim 17 \text{ \AA}$ (see ratio of data/model)¹². Table 5 summarizes the parameter values of the model with and without the thermal component, at rest (i.e., 0 km s^{-1}) and with the best-fit outflow velocity. We present in Figure 8 a high resolution (bin size 25 m\AA) version of our best-photoionization model plotted over the spectrum of MR 2251–178 (in the most interesting range to search for spectral lines, $\sim 1 - 40 \text{ \AA}$). Here we fix the velocity outflow to the best-fit value found above (i.e., -1100 km s^{-1}) and allowed the others parameters free to vary (i.e., $\Gamma_{\text{x}} = 1.64^{+0.03}_{-0.02}$, $N_{\text{H}} = 1.82^{+0.26}_{-0.22} \times 10^{21} \text{ cm}^{-2}$, $\log(\xi) = 0.57^{+0.09}_{-0.13}$, $kT = 95.2^{+3.3}_{-3.2} \text{ eV}$). We use our best-fit featureless continuum (but including bound-free transitions) as the underlying continuum for the search for possible spectral lines (also plotted in Figure 8), discussed in the next section.

3.4.2. Absorption lines

There are several coincidences between the theoretical prediction about where a line is located, and deviations of the data from the fit continuum (the XSTAR featureless global continuum described above). In order to seek for narrow absorption features (in a systematic way) in the spectrum, we use a finer binned spectrum (bin size 25 m\AA). We use the following detection criteria:

1. The counts present in the data must deviate from the fit continuum by at least 1σ . As underlying continuum, we use the best-fit global featureless continuum, described above. We use a global continuum fit because in that way we are less sensitive to local noise in the spectrum¹³.

¹² In order to see if a multicomponent warm absorber system is supported by the data we repeat the above procedure adding a second warm absorber system to the models, without (X_5) and with the blackbody (X_6). In general the data do not well constrain the parameters of the second component. And in any case, no significant improvement is seen by adding a second component to our model (i.e, $\chi^2 \approx 707$, $\Delta\chi^2 \approx 6$ better than X_4), and we do not discuss this model further.

¹³As a test of the robustness of our results, we have also determined the continuum locally around the

2. The FWHM (within errors) of the line should not be significantly smaller than the instrumental FWHM, at the correspondent wavelength.

Not as a criterion, but as an extra piece of statistical evidence for the presence of lines, we use the maximum likelihood ratio test (MLR) to compare the continuum model with the continuum+line model, and compute the line significance (see Table 6 column 4). $P(\geq T)$ is the probability that one would select the more complex model (continuum+line) when in fact the null hypothesis is correct (continuum alone). We set a lower threshold of $P(\geq T) < 0.01$ (not accounting for number of trials). In fact, the four features which passed criteria 1 and 2 also had $P(\geq T)$ below this threshold (see Band et al. 1997, for justification of using the MLR test).

A list of candidate absorption lines is given in Table 6. We measure the center (column 1), and the width (in terms of σ [in km s^{-1}], column 2) of each spectral structure using the best-fit continuum described above.

Figure 10 shows different portions of the spectrum containing absorption lines. Among these lines, we only report measurements from four lines (Table 7), located in a region where the calibration of the LETGS is reliable and its sensitivity is high enough to report 90 % confidence limits on their errors. Deviations $\geq 1\sigma$, but have FWHM too low to be reported as individual lines are still marked in the figure (σ -panel), but are not discussed here any further.

The measurements of the line parameters along with their identification is given in Table 7. In the first column we have the center of the line, and in the second column the equivalent width of the line (EW) in milli-angstroms, computed with:

$$\text{EW} = \int \left[1 - \frac{F_g(\lambda)}{F_c(\lambda)} \right] d\lambda, \quad (2)$$

where $F_g(\lambda) = F_c(\lambda)(1 - \tau_0 \exp[-\frac{(\lambda-\lambda_0)^2}{(2\sigma^2)}])$, $F_c(\lambda)$ is the continuum at the wavelength λ , τ_0 is the depth at the center of the line, σ is the measured width in units of \AA , and λ_0 is the wavelength of the line in \AA (at the core). The EW uncertainties are computed using the lower and upper limits of τ_0 and σ (i.e, $\text{EW}_{\min} = \text{EW}[\tau_{\min}, \sigma_{\min}]$ and $\text{EW}_{\max} = \text{EW}[\tau_{\max}, \sigma_{\max}]$). In the fourth column we give the blueshift of the line (in km s^{-1}). All these are resonance

line. The continuum was fit locally ($\pm 0.5 \text{\AA}$) as a power-law. We find that all four key line candidates are still present when a local continuum is used. To give an example: the equivalent width of the K_β line of N VI (see Table 7) changes from $55^{+90}_{-30} \text{ m\AA}$ to $\approx 70 \text{ m\AA}$, when using a local continuum. The measurements of the other three lines are unaffected by the local continuum fit.

lines, product of electric dipole transitions with the form $1s - np$ for C and $1s^2 - 1snp$ for N ions.

We discuss the issue of line identification in two step. (1) As a first (simplifying) step we assume, that the spectrum is dominated by only one main warm absorber, and that the column density and ionization parameter from the global fit to the X-ray spectrum characterize this main warm absorber reasonably well. Then, this best-fit global warm absorber model guides us in identifying the absorption lines seen in the spectrum. In this first step, we only consider line identification with transitions, which are actually being predicted to be strong (i.e., detectable) by this photoionization model. If no line feature at zero velocity was predicted by the model, we allowed for a range of velocities (up to \sim few thousand km/s - a range of outflow velocities commonly observed in known warm absorbers). That procedure resulted in the line identification reported in Table 7. To give an example of a possible alternative identification, we compare the strength of the line N VI at 24.9 Å (1s-2p, the one identified in Table 7) with a potential alternative identification, the line N VII at 24.8 Å. The former line is much stronger than the latter: The ratio of optical depth at the core is $\tau(\text{N VI})/\tau(\text{N VII}) \approx 8$, for our best-fit global ionization parameter of $\log(\xi) = 0.6$. At this $\log(\xi)$, there is almost 3.5 times more N^{+5} than N^{+6} .

Assuming the one-absorber model is correct, the predicted strongest lines are the four line candidates presented in Table 7. However, we find that lines coming from the same ion are at different outflow velocity. This is a problem at the moment, and opens up a second possibility, which we examined in a second step: (2) the possibility that we see several different warm absorber components each with a different outflow velocity, and each characterized by a potentially different column density and ionization parameter. The data quality, a single grating exposure of only 80 ks, does *not* allow to fit such a four-component absorber with so many free parameters. Therefore in step (2) we made the (simplifying) assumption that the four identified lines are all at the same velocity. We therefore assumed that all four lines are at zero velocity or at velocities up to $\approx 500 \text{ km s}^{-1}$, in particular. Independent of any warm absorber model (i.e., any specific ξ and N_H), we searched line lists to find any consistent line identifications for the four lines, fixing their wavelengths to the quasar rest-frame (i.e., assuming zero velocity), or allowing velocities up to $\approx 500 \text{ km s}^{-1}$. In that case, no line counterparts can be identified.

We therefore continue with solution (1), and discuss some implications of this solution. Since most warm absorbers are not at rest, in order to identify lines, we allowed for a range of outflow velocities, from $0 - 5000 \text{ km s}^{-1}$. We find that not all of the absorption line candidates are at the same outflow velocity, but we preliminary identify 3 velocity systems at $\sim -600 \text{ km s}^{-1}$, -2000 km s^{-1} , and $\sim -3,000 \text{ km s}^{-1}$. Further discussion of these three

components, and a comparison with UV observations is provided in §5.

4. Variability in the band (0.6 – 1) keV

The region $\sim (0.6 - 1)$ keV in the spectrum of MR 2251–178 is complex, due to the presence and blending of three features: the Fe UTA, and the K-edges of oxygen O VII and O VIII. As a first step, we investigate temporal changes assuming the spectrum is actually dominated by the O VII and O VIII edges. Later in §5.2, we carefully discuss the variability of the spectrum based on a photoionization model, which includes a proper treatment of these features including the UTA self-consistently. First, we split the observation in four (equally distributed, ≈ 11 ks of GTI) time intervals (1-4) and applied a `p1 × 2-edges` model to each set of data. By fitting this model (with the edges energy fixed at the values of O VII and O VIII K-edges, 739 and 871 eV respectively), we are able to notice changes (in time) around the bound-free features, at ~ 0.69 keV for O VII and 0.81 keV for O VIII in the observed frame which in turn modify the parameter values of the model (see Table 8). To quantify these changes we looked at the parameters of the model at each time interval. Due to the low S/N of the data these measurements have large errors. Nevertheless, one real inconsistency is seen in the depth of the O VIII edge (τ_{OVIII}) from time interval (1) to (3): approximately a factor of 3.4 in τ_{OVIII} leads to a change in the count rate level of $\approx 20\%$, in the vicinity of the edge. Almost no change is seen in τ_{OVII} , being consistently about the mean best-fit value found before; $\tau_{\text{OVII}} \approx 0.6$.

We caution that the edge model is a too simple representation of the spectrum in the (0.6–1) keV range, where also the UTAs are located. Therefore, we do not draw any physical implications from it. We discuss a more physical photoionization model in §5.2.

5. Discussion

In this section we discuss the physical implications of our measurements, which allow us to draw conclusions about the kinematics of the outflowing gas, ionization state of the warm absorber, and variability of the absorption structure around the oxygen edges seen in the spectrum of MR 2251–178.

5.1. Identification of absorption lines

Identification of absorption lines in the X-ray spectra of AGN is important because these lines carry a wealth of information on the physical conditions in the ionized gas, and its link to other components of the active nucleus.

We have systematically searched for absorption and emission line features in the X-ray spectrum of MR 2251–178, and have identified four absorption line candidates corresponding to transitions in the ions C VI and N VI. These lines, if real, would imply a rather complex velocity field of the absorber, with lines from the same ion indicating different outflow velocities. In particular, it is of our concern the lack of corresponding absorption from the element Oxygen¹⁴. In case of solar abundances of the ionized gas, Oxygen absorption features are expected and have been detected in several AGN with warm absorbers (e.g., Kaastra et al. 2000; Sako et al. 2001; Lee et al. 2001; Blustin et al. 2003; Netzer et al. 2003; Fields et al. 2007; Costantini et al. 2007; Krongold et al. 2007) even though few of them with well-measured column densities. On the other hand, it has also been found that warm absorbers are complex, stratified, multi-component, time-variable, and possibly of non-solar abundances, and the same may well hold for MR 2251–178. With these cautious comments in mind, we briefly discuss implications of the line candidates we find. Ultimately, deeper grating observations are needed to study the absorption line features and their temporal evolution.

Independent information on the presence and velocity fields of ionized absorption components comes from a comparison of X-ray with UV observations. Firstly, in our LETG spectrum we identified a candidate gas component outflowing at a velocity $v \sim -600$ km s⁻¹, as indicated by the C VI $\lambda 33.736$ line. This is consistent with UV measurements. The UV spectrum of MR 2251–178 provides evidence for an absorbing system at an outflow velocity of $v = -580$ km s⁻¹ (Kaspi et al. 2004). This component is seen through the O VI $\lambda 1032, 1038$ and Ly $_{\alpha}$ lines, observed with the STIS on board HST. Also (and reported by the same authors), this component is in accordance with the velocity of ≈ -600 km s⁻¹, reflected by the Ly $_{\beta}$ line, observed with FUSE. This is interesting, because it confirms the scenario where UV and X-ray absorber systems could be physically related (Mathur et al. 1998). However, the centroid of our X-ray line candidate is measured with an uncertainty that also allows to relate this X-ray absorption system with the average outflow velocity of ~ -300 km s⁻¹ reported by Monier et al. (2001) using the Ly $_{\alpha}$, N V $\lambda 1240$, and C IV $\lambda 1549$

¹⁴we have carefully searched at the location of O VII at $\lambda 21.8$ Å, and cannot identify any feature. This is consistent with Gibson et al. (2005) while Kaspi et al. (2004) report some Oxygen absorption features at $\sim 16 - 22$ Å in the RGS spectrum of MR 2251–178 (their Table 3), albeit with low significance.

lines in the ultraviolet (UV) band (with the *HST-Faint Object Spectrograph* observation of MR 2251–178).

For the computation of the mass-outflow rate, we assume that the outflowing material in MR 2251–178 forms a spherical shell ($n \sim r^2$) expanding at velocity v . Using the approximation $N \sim nr$, we can write:

$$\dot{M}_{\text{out}} = 4\pi\mu_H N r v f_{\text{cov}}, \quad (3)$$

or

$$\dot{M}_{\text{out}} \approx 0.048 N_{21} r_{18} \left(\frac{v}{1000 \text{ km s}^{-1}} \right) f_{\text{cov}} M_{\odot} \text{ yr}^{-1}, \quad (4)$$

where μ_H is the mean mass per H atom (equal to $\frac{m_p}{0.7}$), N_{21} is the column density of the material in units of 10^{21} cm^{-2} , r_{18} is the distance of the gas in units of 10^{18} cm , and f_{cov} is the covering factor ($\Omega/[4\pi]$). Using our best-fit $N_{\text{H}} \sim 10^{21.35}$, an outflow velocity $v = 1100 \text{ km s}^{-1}$, at a distance of $1.5 \times 10^{18} \text{ cm}$ (distance chosen for illustrative purposes) we have a mass-loss rate $\dot{M}_{\text{out}} \approx 0.18 f_{\text{cov}} M_{\odot} \text{ yr}^{-1}$.

In Table 9 is quoted our estimate of the mass-loss rate of the LETG X-ray warm absorber system compared with previous values. To compute the mass-loss rate, Gibson et al. (2005) used a high-velocity outflow $v \sim 13,000 \text{ km s}^{-1}$, concluding that \dot{M}_{out} could significantly exceed the accretion rate ($\sim 0.2 M_{\odot} \text{ yr}^{-1}$), by $\sim 1 - 2$ orders of magnitude, even taking the Fe xxvi line (see Table 7 of that paper). On the other hand, Monier et al. (2001), using an outflow velocity of 300 km s^{-1} , estimate a mass-loss rate of $\sim 0.9 M_{\odot} \text{ yr}^{-1}$ for a 10% covering factor, putting this value close to the accretion rate. Our computation of \dot{M}_{\odot} is more in agreement with the value found by these last authors. The kinematic energy rate carried away by the flow spans $\approx (0.07 - 1) \times 10^{42} f_{\text{cov}} \text{ erg s}^{-1}$.

5.2. Absorption variability during the observation

Warm absorbers are known to vary on short and long time scales. We find indications for variability during the LETG observation of MR 2251–178 in the wavelength range that includes the oxygen absorption edges and the Fe UTA features. Both, the UTAs (e.g., Krongold et al. 2005) and/or the absorption edges could be variable. Mechanisms of variability include changes of the ionization state of the absorber to changes in the ionizing continuum, changes of the internal structure of the absorber, and clouds crossing our line of sight.

In order to find clues on the variability mechanism, we have fit our most successful warm absorber photoionization model (model X_4 ; i.e., `(pl+bb) × xstar`, with $v_{\text{out}} = -1100 \text{ km}$

s⁻¹) separately to the four subsets of the total observation (Fig. 2). We have explored the effects of variable column density, ionization parameter, and intensity of the continuum (black body and powerlaw) spectral components. The strongest effect is a change in column density of the ionizing material in epoch (3); formally requiring (at $\gtrsim 6\sigma$) a smaller column density in order to fit successfully that epoch (Fig. 11). In order to re-check whether the data do indicate variability between the different epochs, we have used the best-fit model of epoch (1) and compared it to the data of epoch (3). In the comparison, we have fixed all the parameters (of our model X_4) to those derived for epoch (1), and then inspected the residuals during epoch (3). Clear deviations are seen (Figure 12), demonstrating independently the presence of spectral changes throughout the observation.

Changes in the luminosity would affect the ionization state of the absorber, but the average countrate or MR2251-178 does not vary throughout the observation. Taken at face value, a true change in column density would require a change in density and/or thickness of the absorber, and we first briefly comment on this possibility. Assuming the thickness of the absorber has not changed in such a short time, the density of the absorber would need to change by a factor of 3 to account for the change in N_H between periods (1) and (3). However, changing the density of the whole extended gas (or a fraction of the gas by a large amount), is not easy in such a short time scale. Re-arrangements of clouds crossing our line-of-sight would have to occur within ~ 10 ks, which is very unlikely. Alternatively we may see non-equilibrium ionization effects in the gas, in which the material responds with some time delay in a complicated way to previous variability in the ionizing continuum, which was not within our observation time window. Deeper observations with longer time bases are required to investigate these possibilities further.

6. Conclusions

The measured (0.1 – 2) keV flux $f_{(0.1-2 \text{ keV})} = 2.58_{-0.03}^{+0.04} \times 10^{-11}$ ergs cm⁻² s⁻¹ implies that MR 2251–178 is in a relatively low state. The soft X-ray luminosity amounts to $L_{(0.1-2 \text{ keV})} = 2.54 \times 10^{44}$ erg s⁻¹.

We did not find any strong evidence for the presence of an extra cold material with column density of $N_H \sim 10^{21}$ cm⁻² toward MR 2251–178 (if part of this is located along our line of sight). Based on different spectral fits, we set the upper limit of this component to $N_{\text{cold}} \approx 1.2 \times 10^{20}$ cm⁻².

As for previous observations of MR 2251–178, power-law plus blackbody does not provide a successful fit to the X-ray spectrum. The addition of a warm absorber improves the

fit significantly.

Based on XSTAR photoionization modelling, we find the observation to be consistent with ionized absorbing material in our line of sight, column density $N_{\text{H}} \approx 2 \times 10^{21} \text{ cm}^{-2}$, and an ionization parameter of $\log(\xi) \approx 0.6$. The inclusion of an additional thermal component is important because otherwise: (1) the absorption structure around 18 \AA is not well reproduced, (2) the ionization state of the gas would be higher, bringing a lot of problems in the identification of the atomic line transition. The temperature of the blackbody used to represent this thermal component is $kT \approx 90 \text{ eV}$.

We find four line candidates at moderate confidence level. If these lines are real, their presence would imply three components traveling at velocities $\sim 600, 2000$ and 3000 km s^{-1} . We compute $\dot{M} \sim 0.01 - 0.1 M_{\odot} \text{ yr}^{-1}$ and a kinematic energy of $\sim 10^{40-42} \text{ erg s}^{-1}$, using the C VI and N VI lines outflowing at velocities of $\sim 2000 - 3000 \text{ km s}^{-1}$. Using $f_{\text{cov}} = 0.1$, this value is a factor of ~ 20 less than the accretion rate of the system. However, we caution that these candidates need to be confirmed with future observations. The lack of corresponding oxygen absorption is a problem at present.

We do not find positive evidence for a dusty warm absorber. The spectrum of MR 2251–178 allows us to set an upper limit of $N_{\text{C I}} \approx 2 \times 10^{19} \text{ cm}^{-2}$, and $N_{\text{O I}} \approx 9 \times 10^{19} \text{ cm}^{-2}$, if dusty material is present in the nucleus of MR 2251–178.

We find changes in the absorption structure of MR 2251–178 during the observation, not accompanied by changes in the observed continuum luminosity. Possibly, we see non-equilibrium effects in the ionization of the gas responding to previous changes in luminosity, or changes in density; the true mechanism can only be uncovered with deeper follow-up observations.

We thank the anonymous referee for many constructive comments. The observation would not have been possible to analyze without the enormous effort of the *Chandra* team.

REFERENCES

- Anders, E. & Grevesse, N. 1989, *Geochim. Cosmochim. Acta*, 53, 197
- Band, D. L., Ford, L. A., Matteson, J. L., Briggs, M. S., Paciesas, W. S., Pendleton, G. N., & Preece, R. D. 1997, *ApJ*, 485, 747
- Bautista, M. A. & Kallman, T. R. 2001, *ApJS*, 134, 139

- Behar, E., Sako, M., & Kahn, S. M. 2001, *ApJ*, 563, 497
- Bergeron, J., Dennefeld, M., Boksenberg, A., & Tarenghi, M. 1983, *MNRAS*, 202, 125
- Beuermann, K., Burwitz, V., & Rauch, T. 2006, *A&A*, 458, 541
- Blustin, A. J., Branduardi-Raymont, G., Behar, E., Kaastra, J. S., Kriss, G. A., Page, M. J., Kahn, S. M., Sako, M., & Steenbrugge, K. C. 2003, *A&A*, 403, 481
- Brinkman, B. C., Gunsing, T., Kaastra, J. S., van der Meer, R., Mewe, R., Paerels, F. B., Raassen, T., van Rooijen, J., Braeuninger, H. W., Burwitz, V., Hartner, G. D., Kettenring, G., Predehl, P., Drake, J. J., Johnson, C. O., Kenter, A. T., Kraft, R. P., Murray, S. S., Ratzlaff, P. W., & Wargelin, B. J. 2000, in *Proc. SPIE Vol. 4012, p. 81-90, X-Ray Optics, Instruments, and Missions III*, Joachim E. Truemper; Bernd Aschenbach; Eds., ed. J. E. Truemper & B. Aschenbach, 81–90
- Costantini, E., Kaastra, J. S., Arav, N., Kriss, G. A., Steenbrugge, K. C., Gabel, J. R., Verbunt, F., Behar, E., Gaskell, C. M., Korista, K. T., Proga, D., Quijano, J. K., Scott, J. E., Klimek, E. S., & Hedrick, C. H. 2007, *A&A*, 461, 121
- Crenshaw, D. M., Kraemer, S. B., & George, I. M. 2003, *ARA&A*, 41, 117
- Fields, D. L., Mathur, S., Krongold, Y., Williams, R., & Nicastro, F. 2007, *ApJ*, 666, 828
- Ganguly, R., Charlton, J. C., & Eracleous, M. 2001, *ApJ*, 556, L7
- George, I. M., Turner, T. J., Netzer, H., Nandra, K., Mushotzky, R. F., & Yaqoob, T. 1998, *ApJS*, 114, 73
- Gibson, R. R., Marshall, H. L., Canizares, C. R., & Lee, J. C. 2005, *ApJ*, 627, 83
- Grevesse, N., Noels, A., & Sauval, A. J. 1996, in *Astronomical Society of the Pacific Conference Series*, 117
- Gu, M. F., Holczer, T., Behar, E., & Kahn, S. M. 2006, *ApJ*, 641, 1227
- Halpern, J. P. 1984, *ApJ*, 281, 90
- Kaastra, J. S., Mewe, R., Liedahl, D. A., Komossa, S., & Brinkman, A. C. 2000, *A&A*, 354, L83
- Kaspi, S., Netzer, H., Chelouche, D., George, I. M., Nandra, K., & Turner, T. J. 2004, *ApJ*, 611, 68

- Komossa, S. 2001, *A&A*, 367, 801
- Komossa, S. & Bade, N. 1998, *A&A*, 331, L49
- Komossa, S. & Fink, H. 1997, *A&A*, 322, 719
- Komossa, S. & Hasinger, G. 2003, in *XEUS - studying the evolution of the hot universe*, ed. G. Hasinger, T. Boller, & A. N. Parmer, 285
- Krongold, Y., Nicastro, F., Brickhouse, N. S., Elvis, M., Liedahl, D. A., & Mathur, S. 2003, *ApJ*, 597, 832
- Krongold, Y., Nicastro, F., Brickhouse, N. S., Elvis, M., & Mathur, S. 2005, *ApJ*, 622, 842
- Krongold, Y., Nicastro, F., Elvis, M., Brickhouse, N., Binette, L., Mathur, S., & Jiménez-Bailón, E. 2007, *ApJ*, 659, 1022
- Lee, J. C., Ogle, P. M., Canizares, C. R., Marshall, H. L., Schulz, N. S., Morales, R., Fabian, A. C., & Iwasawa, K. 2001, *ApJ*, 554, L13
- Leighly, K. M. 2004, *ApJ*, 611, 125
- Lockman, F. J. & Savage, B. D. 1995, *ApJS*, 97, 1
- Macchetto, F., Colina, L., Golombek, D., Perryman, M. A. C., & di Serego Alighieri, S. 1990, *ApJ*, 356, 389
- Markwardt, C. B., Tueller, J., Skinner, G. K., Gehrels, N., Barthelmy, S. D., & Mushotzky, R. F. 2005, *ApJ*, 633, L77
- Mathur, S., Wilkes, B., & Elvis, M. 1998, *ApJ*, 503, L23
- Monier, E. M., Mathur, S., Wilkes, B., & Elvis, M. 2001, *ApJ*, 559, 675
- Morrison, R. & McCammon, D. 1983, *ApJ*, 270, 119
- Nagao, T., Murayama, T., Taniguchi, Y., & Yoshida, M. 2000, *AJ*, 119, 620
- Netzer, H., Kaspi, S., Behar, E., Brandt, W. N., Chelouche, D., George, I. M., Crenshaw, D. M., Gabel, J. R., Hamann, F. W., Kraemer, S. B., Kriss, G. A., Nandra, K., Peterson, B. M., Shields, J. C., & Turner, T. J. 2003, *ApJ*, 599, 933
- Ricker, G. R., Clarke, G. W., Doxsey, R. E., Dower, R. G., Jernigan, J. G., Delvaille, J. P., MacAlpine, G. M., & Hjellming, R. M. 1978, *Nature*, 271, 35

Sako, M., Kahn, S. M., Behar, E., Kaastra, J. S., Brinkman, A. C., Boller, T., Puchnarewicz, E. M., Starling, R., Liedahl, D. A., Clavel, J., & Santos-Lleo, M. 2001, *A&A*, 365, L168

Tarter, C. B., Tucker, W. H., & Salpeter, E. E. 1969, *ApJ*, 156, 943

Table 1. *Chandra* Observation Log of MR 2251–178.

Sequence Number	UT Start	UT End	Time (ks)
700405	2002 Dec 23, 16:35	2002 Dec 24, 14:54	78.5

Table 2. Cold absorption fit results

N_{H}^{a}	Γ_{x}	Norm ^h	$\Gamma_{\text{x}}(2)$	Norm ^h (2)	kT^{i}	Norm ^j	$\chi^2_{\nu}/(\text{d.o.f})$
$1.68^{+0.07}_{-0.07}$ ^b	$1.79^{+0.02}_{-0.02}$	$5.34^{+0.06}_{-0.06}$	2.55/306
2.77 ^c	$1.94^{+0.02}_{-0.02}$	$5.65^{+0.06}_{-0.06}$	3.00/307
3.27 ^d	$2.00^{+0.02}_{-0.02}$	$5.78^{+0.06}_{-0.06}$	3.40/307
3.77 ^e	$2.05^{+0.02}_{-0.02}$	$5.91^{+0.06}_{-0.06}$	3.85/307
$\lesssim 10^{-6}$ ^b	$1.52^{+0.02}_{-0.02}$	$4.70^{+0.07}_{-0.05}$	$80.3^{+3.0}_{-1.3}$	$1.04^{+0.03}_{-0.05}$	1.64/304
$1.24^{+0.10}_{-0.09}$ ^b	$3.47^{+0.03}_{-0.03}$	$1.20^{+0.03}_{-0.03}$	$1.41^{+0.03}_{-0.03}$	$3.97^{+0.06}_{-0.06}$	1.81/304
1.74 ^f	$3.70^{+0.03}_{-0.03}$	$1.04^{+0.03}_{-0.03}$	$1.44^{+0.03}_{-0.02}$	$4.16^{+0.06}_{-0.06}$	1.81/305
2.24 ^g	$3.94^{+0.03}_{-0.03}$	$0.91^{+0.02}_{-0.02}$	$1.47^{+0.03}_{-0.02}$	$4.34^{+0.06}_{-0.06}$	1.84/305

Note. — The error parameters are 90 % confidence limits. (a) Absorber column density in units of 10^{20} cm^{-2} . (b) Free parameter. (c) Fixed to Galactic value. (d) Fixed to Galactic value plus ΔN_{H} , where $\Delta N_{\text{H}} = 5 \times 10^{19} \text{ cm}^{-2}$. (e) Fixed to Galactic value plus $2 \times \Delta N_{\text{H}}$. (f) Extra absorber column density (shifted by $z = 0.06398$, model **zphabs** in XSPEC), fixed to the best value plus ΔN_{H} . The fit is corrected by the Galactic absorption. (g) Extra absorber column density (shifted by $z = 0.06398$, model **zphabs** in XSPEC), fixed to the best value plus $2 \times \Delta N_{\text{H}}$. The fit is corrected by the Galactic absorption. (h) Powerlaw normalization, $\times 10^{-3}$ photons $\text{keV}^{-1} \text{cm}^{-2} \text{s}^{-1}$ at 1 keV. (i) Temperature of the blackbody in eV. (j) $\times 10^{-6}$ in units of L_{39}/D_{10}^2 , where L_{39} is the luminosity of the source in units of $10^{39} \text{ erg s}^{-1}$, and D_{10} the distance to the source in units of 10 kpc.

Table 3. Results from simple model fits

Model ^b	Γ_x	Norm ^c	$\tau_{\text{O VII}}$	$\tau_{\text{O VIII}}$	kT ^d	Norm ^e	$\chi^2_{\nu} / (\text{d.o.f})$
[1]	$1.94^{+0.02}_{-0.02}$	$5.65^{+0.06}_{-0.06}$	3.00/(307)
[2]	$1.53^{+0.02}_{-0.02}$	$4.73^{+0.06}_{-0.06}$	$81.5^{+2.0}_{-2.0}$	$9.94^{+0.38}_{-0.38}$	1.63/(305)
[3]	$1.92^{+0.02}_{-0.02}$	$6.53^{+0.07}_{-0.07}$	$0.56^{+0.05}_{-0.04}$	$0.22^{+0.05}_{-0.04}$	1.38/(305)
[4]	$1.85^{+0.02}_{-0.02}$	$6.35^{+0.07}_{-0.07}$	$0.51^{+0.05}_{-0.04}$	$0.21^{+0.05}_{-0.04}$	$44.1^{+3.0}_{-3.0}$	$5.57^{+0.92}_{-0.92}$	1.25/(303)

Note. — All the models include absorption fixed at the Galactic value of $N_{\text{H}} = 2.77 \times 10^{20} \text{ cm}^{-2}$. The error parameters are 90 % confidence limits. (b): Model [1]: **p1**; [2]: **p1+bb**; [3]: **p1×2 edges**; [4]: **(p1+bb)×2 edges**; **p1=powerlaw**; **bb=blackbody**. (c) Powerlaw normalization, in units of $10^{-3} \text{ photons keV}^{-1} \text{ cm}^{-2} \text{ s}^{-1}$ at 1 keV. (d) Temperature of the blackbody in eV. (e) $\times 10^{-5}$ in units of L_{39}/D_{10}^2 , where L_{39} is the luminosity of the source in units of $10^{39} \text{ erg s}^{-1}$, and D_{10} the distance to the source in units of 10 kpc.

Table 4. Dusty warm absorber fit results

Γ_x	Norm ^b	$\tau_{\text{O VII}}$	$\tau_{\text{O VIII}}$	$\tau_{\text{C I}}$	$\tau_{\text{O I}}$	$\chi^2_{\nu}/(\text{d.o.f})^e$
$1.92^{+0.02}_{-0.02}$	$6.53^{+0.07}_{-0.07}$	$0.55^{+0.05}_{-0.04}$	$0.23^{+0.04}_{-0.05}$	$0.02^{+0.06}$	$0.05^{+0.04}_{-0.04}$	1.22/585
$1.93^{+0.02}_{-0.02}$	$6.58^{+0.07}_{-0.07}$	$0.55^{+0.05}_{-0.04}$	$0.23^{+0.05}_{-0.04}$	0.06 ^c	$0.06^{+0.04}_{-0.04}$	1.22/586
$1.93^{+0.02}_{-0.02}$	$6.58^{+0.07}_{-0.07}$	$0.54^{+0.05}_{-0.04}$	$0.24^{+0.05}_{-0.04}$	$0.04^{+0.06}$	0.09 ^d	1.22/586

Note. — The error parameters are 90 % confidence limits. (b) Powerlaw normalization, $\times 10^{-3}$ photons $\text{keV}^{-1}\text{cm}^{-2}\text{s}^{-1}$ at 1 keV. (c) Fitting, enforcing $\tau_{\text{C I}} = 0.08$, and $\tau_{\text{O I}}$ free. (d) Fitting, enforcing $\tau_{\text{O I}} = 0.09$, and $\tau_{\text{C I}}$ free. (e) In order to search for fine features, we used a larger number of bins in the fit, 50 counts from the source per bin. For comparison the best fit model of the `p1 × 2edges` model (using this data) gives $\chi^2_{\nu} = 1.22/(\text{d.o.f}=587)$.

Table 5. Fit results for photoionization models.

Parameter	X ₁	X ₂	X ₃	X ₄
Γ_x	$1.96^{+0.02}_{-0.02}$	$1.66^{+0.02}_{-0.02}$	$1.97^{+0.02}_{-0.02}$	$1.66^{+0.02}_{-0.02}$
Norm ^a	$6.84^{+0.07}_{-0.07}$	$5.42^{+0.07}_{-0.07}$	$6.82^{+0.07}_{-0.07}$	$5.38^{+0.07}_{-0.07}$
kT (eV)	...	$89.9^{+2.6}_{-2.5}$...	$89.5^{+2.5}_{-2.5}$
Norm _{bb} ^b	...	$10.21^{+0.42}_{-0.42}$...	$10.29^{+0.44}_{-0.40}$
N_H ^c	$4.77^{+0.31}_{-0.29}$	$2.44^{+0.13}_{-0.29}$	$4.28^{+0.29}_{-0.21}$	$2.25^{+0.28}_{-0.25}$
$\log(\xi)$	$1.83^{+0.06}_{-0.06}$	$0.64^{+0.11}_{-0.06}$	$1.72^{+0.07}_{-0.07}$	$0.63^{+0.06}_{-0.06}$
v_{out} ^d	0	0	-340^{+120}_{-20}	-1100^{+60}_{-210}
$\chi^2_{\nu}/(\text{d.o.f})$	1.54/(587)	1.27/(585)	1.52/(586)	1.22/(584)

Note. — (a) Powerlaw normalization, in units of $\times 10^{-3}$ photons $\text{keV}^{-1}\text{cm}^{-2}\text{s}^{-1}$ at 1 keV. (b) $\times 10^{-5}$ in units of L_{39}/D_{10}^2 , where L_{39} is the luminosity of the source in units of 10^{39} erg s^{-1} , and D_{10} the distance to the source in units of 10 kpc. (c) Column density of the ionized material in units of $\times 10^{21}$ cm^{-2} . (d) Outflow velocity of the ionized gas in units of km s^{-1} . Models X₁ – X₄ are described in the text (see section 3.4.1).

Table 6. Gaussian absorption line candidates

Obs. λ (Å)	σ_{measured} (km s ⁻¹)	σ_{LETG} (km s ⁻¹)	MLR $P(\geq T)$
26.34 ^{+0.03} _{-0.01}	160 ⁺¹⁰⁰ ₋₉₀	242	7.38×10^{-3}
30.09 ^{+0.02} _{-0.02}	190 ⁺¹³⁰ ₋₉₀	212	1.13×10^{-3}
30.32 ^{+0.03} _{-0.02}	280 ⁺²⁹⁰ ₋₁₂₀	210	7.06×10^{-4}
35.83 ^{+0.03} _{-0.03}	220 ⁺¹³⁰ ₋₁₁₀	178	1.17×10^{-2}

Note. — Error parameters are 90 % confidence limits. The final significance is less than the one shown in column 4, since the number of trials is not considered. The MLR test is described in Section 3.4.2.

Table 7. Identification of absorption line candidates

λ_{obs} (\AA)	EW (m\AA)	Ion and atomic transition	λ_{lab} (\AA)	v_{shift} (km s^{-1})
$26.34^{+0.03}_{-0.01}$	55^{+90}_{-30}	N VI $1s^2 \ ^1S - 1s3p^1P^o$	24.914	-2030^{+360}_{-120}
$30.09^{+0.02}_{-0.02}$	63^{+84}_{-35}	C VI $1s \ ^2S - 3p^2P^o$	28.466	-2080^{+210}_{-210}
$30.32^{+0.03}_{-0.02}$	70^{+76}_{-40}	N VI $1s^2 \ ^1S - 1s2p^1P^o$	28.787	-3220^{+310}_{-210}
$35.83^{+0.03}_{-0.03}$	86^{+98}_{-30}	C VI $1s \ ^2S - 2p^2P^o$	33.736	-580^{+270}_{-270}

Note. — Errors are 90% confidence limits.

Table 8. Variability of the oxygen edges^a

Period	t_{start}^b $\times 10^8$ (s)	t_{end}^b $\times 10^8$ (s)	total counts ($\times 10^4$)	Γ_x	Norm ^c	τ_{O+6}	τ_{O+7}	$\chi^2_{\nu}/(\text{d.o.f})$
(1)	1.57048747	1.570653992	1.8298	$1.90^{+0.04}_{-0.04}$	$6.11^{+0.13}_{-0.13}$	$0.57^{+0.09}_{-0.09}$	$0.09^{+0.08}$	1.19/161
(2)	1.570653993	1.570819941	1.6104	$1.89^{+0.04}_{-0.04}$	$6.58^{+0.14}_{-0.14}$	$0.67^{+0.10}_{-0.09}$	$0.25^{+0.10}_{-0.09}$	1.01/145
(3)	1.570819942	1.570982180	1.7391	$1.91^{+0.04}_{-0.04}$	$6.62^{+0.14}_{-0.14}$	$0.46^{+0.09}_{-0.08}$	$0.31^{+0.09}_{-0.09}$	1.32/159
(4)	1.570982181	1.571276092	1.5842	$1.96^{+0.04}_{-0.04}$	$6.61^{+0.15}_{-0.15}$	$0.57^{+0.10}_{-0.09}$	$0.22^{+0.10}_{-0.09}$	1.39/144

^aThe model includes Galactic absorption of $N_{\text{H}} = 2.77 \times 10^{20} \text{ cm}^{-2}$. The error parameters are 90 % confidence limits computed with the spectrum adaptively binned to have at least 50 counts from the source per bin.

^bIn the detector (original) time. These intervals exclude data from the “bad time intervals” (section 2.1)

^cPowerlaw normalization, in units of $10^{-3} \text{ photons keV}^{-1} \text{ cm}^{-2} \text{ s}^{-1}$ at 1 keV.

Table 9. Outflow masses and kinematic energy rates

Ion ^a	\dot{M} (Monier et al. 2001) ^b [M_{\odot} yr ⁻¹]	\dot{M}^e [M_{\odot} yr ⁻¹]	$\frac{1}{2}\dot{M}v^{2e}$ [erg s ⁻¹]	\dot{M}^f [M_{\odot} yr ⁻¹]	$\frac{1}{2}\dot{M}v^{2f}$ [erg s ⁻¹]
C IV	0.9
Fe XXVI	...	$220f_{\text{cov}}$	$1.1 \times 10^{46}f_{\text{cov}}$
Fe XVII	...	$8900f_{\text{cov}}$	$7.9 \times 10^{47}f_{\text{cov}}$
S XIV	...	$1700f_{\text{cov}}$	$1.6 \times 10^{47}f_{\text{cov}}$
(c)	$0.18f_{\text{cov}}$	$6.7 \times 10^{40}f_{\text{cov}}$
N VI ^d	$0.32f_{\text{cov}}$	$4.0 \times 10^{41}f_{\text{cov}}$
C VI ^d	$0.48f_{\text{cov}}$	$1.4 \times 10^{42}f_{\text{cov}}$

Note. — (a) Ion from which the rates are computed. (b) For a covering factor of 10%. (c) Best-fit outflow velocity found in §3.4 of 1100 km s⁻¹. (d) Using the velocities shown by the lines in Table 7 (and $N_{\text{H}} = 10^{21.35}$ cm⁻²), of ≈ 2000 km s⁻¹, and 3000 km s⁻¹ for N, and C line respectively. (e) From Gibson et al. (2005). (f) Present work.

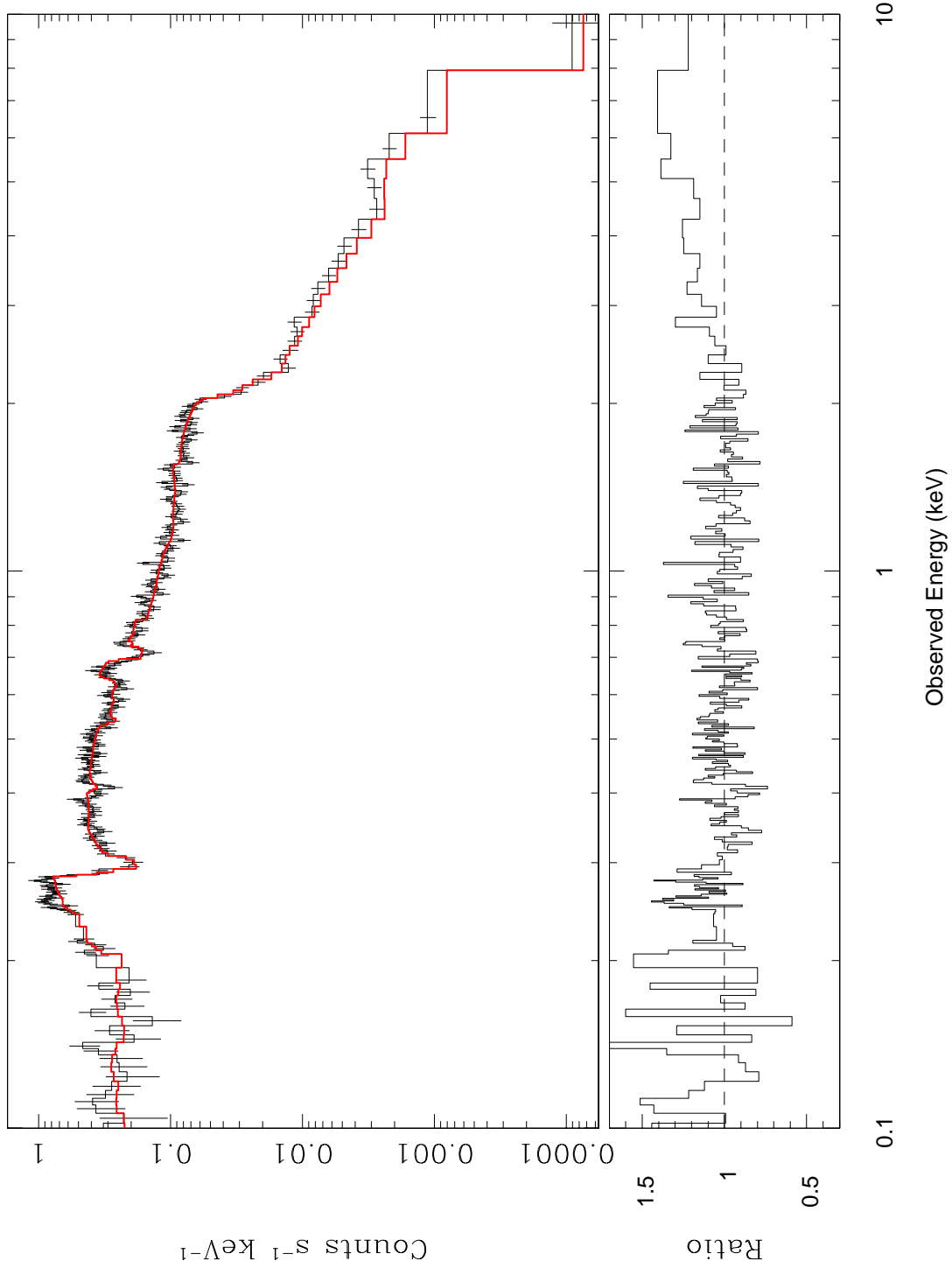


Fig. 1.— 0.1-10 keV LETGS spectrum of MR 2251–178 (observed frame). It is binned to have at least 100 counts from the source per bin. In red the model of a simple absorbed power-law modified by 2 oxygen absorption edges.

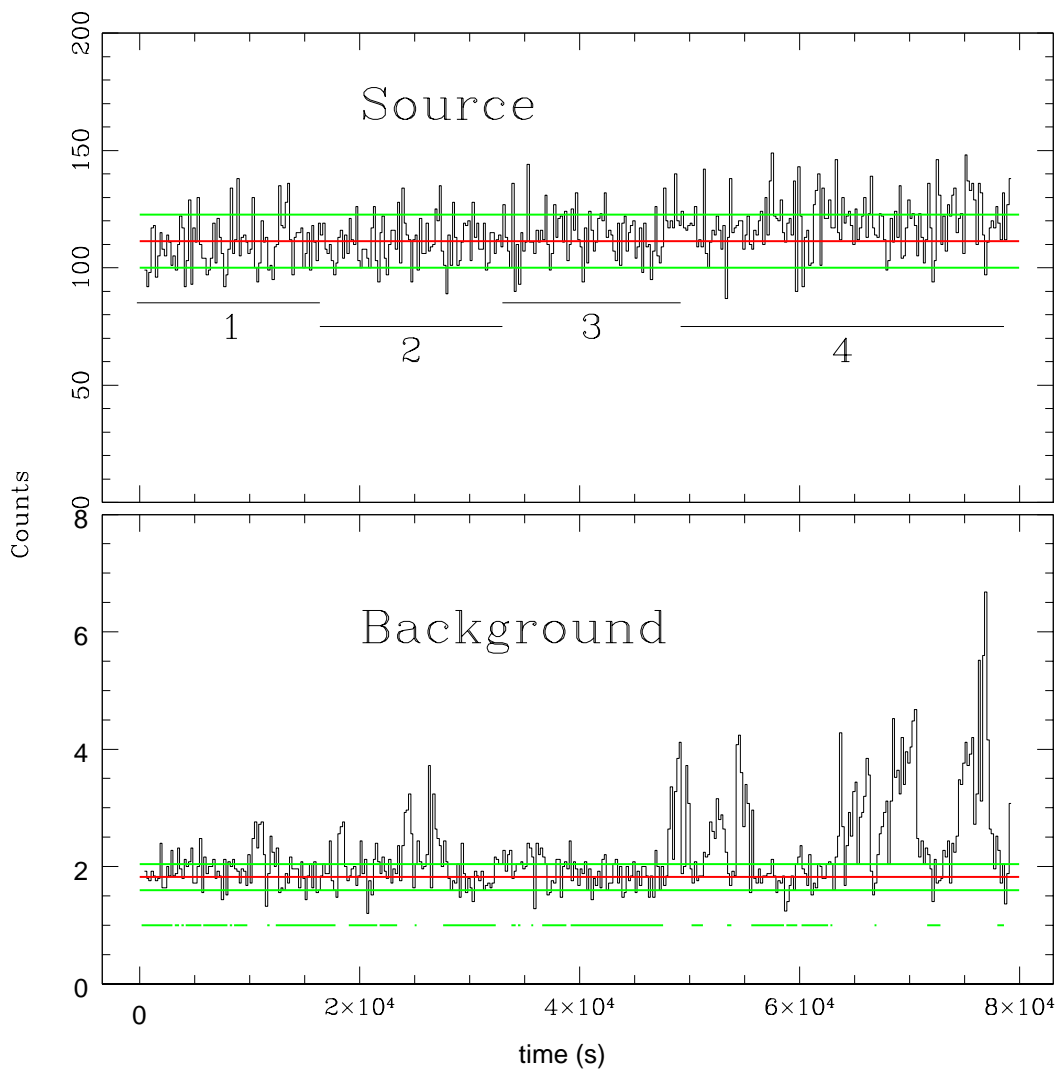


Fig. 2.— Light curves of the source and background (bin size 200 s). The top panel shows, in red, the mean counts of the source. No significant time variability is seen within $\pm 1\sigma$ (green lines). The bottom panel shows strong variability of the background (here, the green lines show $\pm 3\sigma$). The good time intervals are indicated by the interrupted line below the background spectrum. The meaning of intervals (1)-(4) is explained in §4.

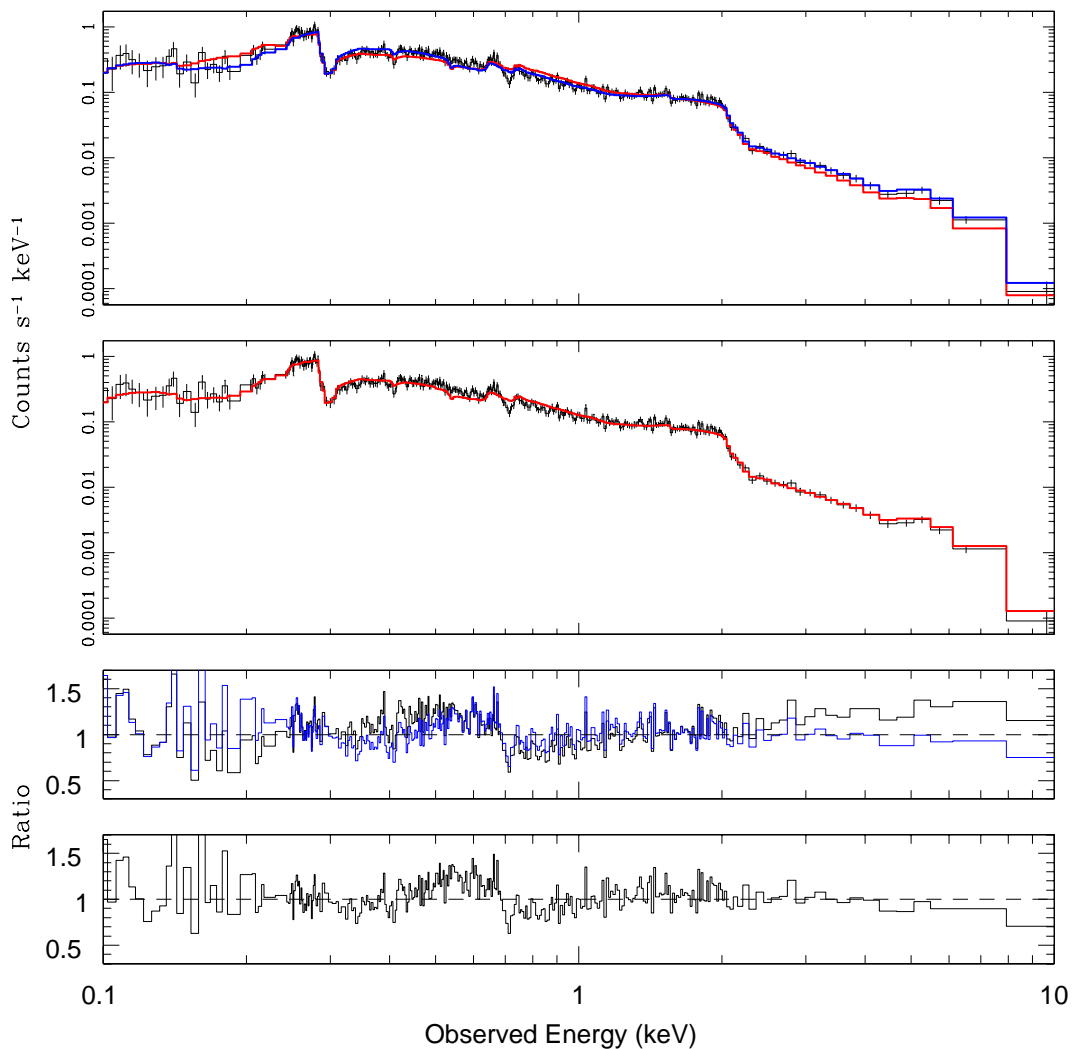


Fig. 3.— LETGS spectrum of MR 2251–178 (positive and negative orders added) in energy space. **Top panel:** The solid red line shows the absorbed power-law fit. The solid blue line is the absorbed `p1+bb` model. **Middle panel:** The solid line is the absorbed two power-law model. **Bottom panels:** Ratios of the composite models to the data: absorbed power-law (black) and blackbody plus power-law (blue), in the bottom panel the ratio for the two power-laws model (*absorbed*, means cold absorption with `zphabs`).

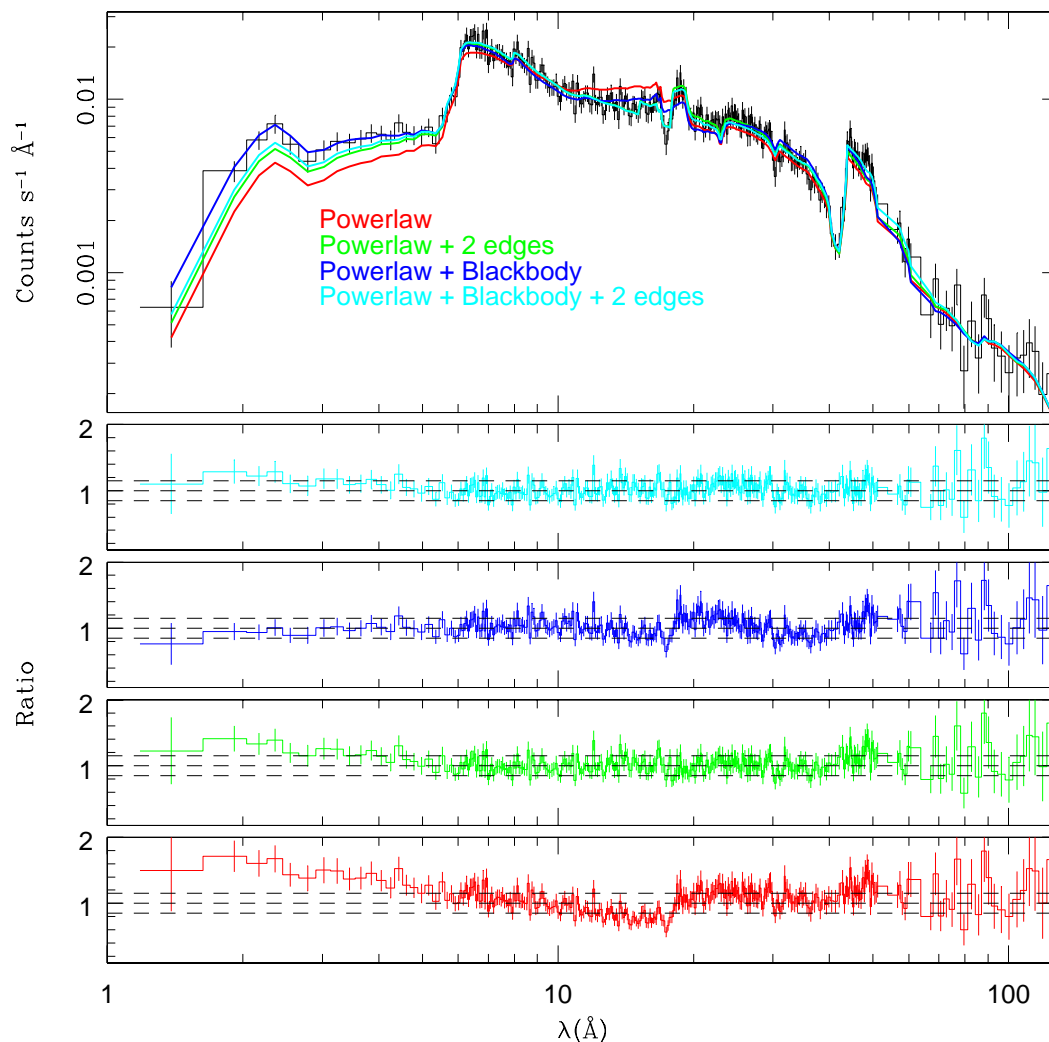


Fig. 4.— LETGS spectrum of MR 2251–178 in the observed frame (positive and negative orders added). It is binned to have at least 100 counts from the source per bin. All the models include the Galactic absorption toward MR 2251–178 (see text). **Top panel:** Solid lines: p1 (red), p1 \times 2 edges (green), p1+bb (dark blue), (p1+bb) \times 2 edges (light blue). The rest of the panels are the ratios of each composite model to the data, represented by their corresponding colors (p1=power-law; bb=blackbody).

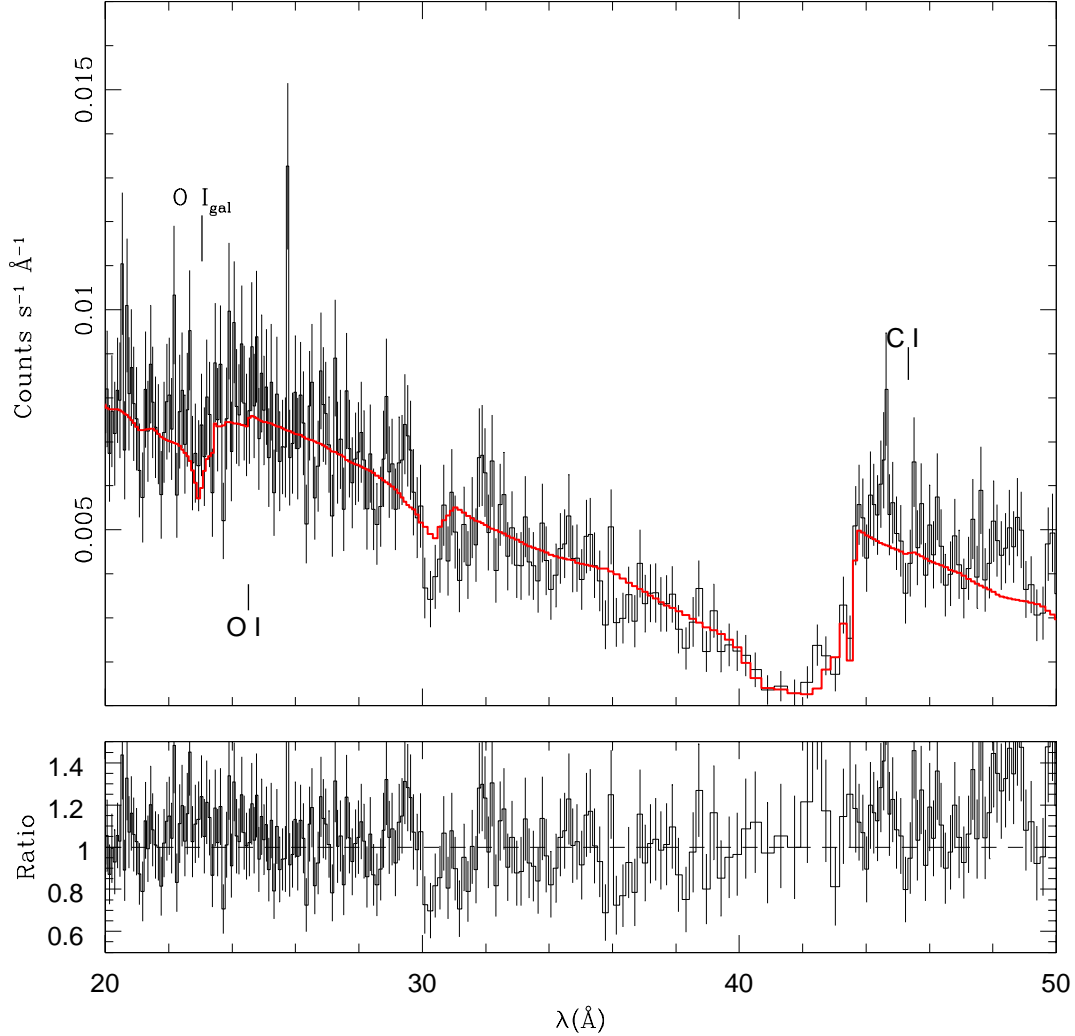


Fig. 5.— Test for the presence of a dusty warm absorber. X-ray spectrum of MR 2251–178 (observed frame), with a power-law model modified by four edges (solid red line). The edges corresponding to the H- and He-like oxygen features are included in the model but they lie off the figure axis. Marked are edges expected from dusty material represented by bound-free transitions of neutral carbon and oxygen, in the observer’s frame. Also marked is the oxygen edge coming from the Galactic absorption toward MR 2251–178.

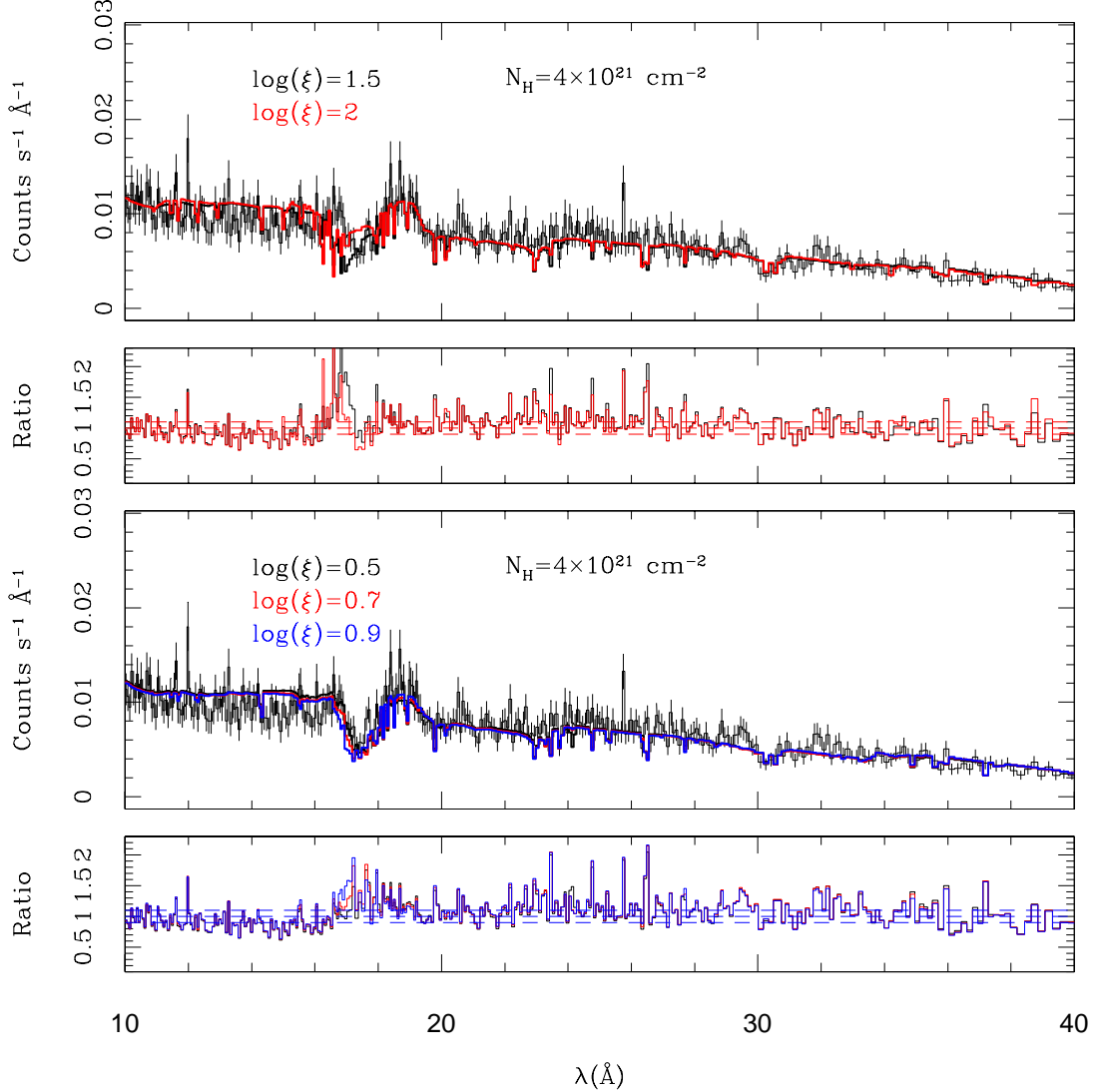


Fig. 6.— 10 – 40 Å spectrum of MR 2251–178 and XSTAR photoionization models of different ionization parameters. We use $N_H = 4 \times 10^{21} \text{ cm}^{-2}$ for illustrative purposes. **Top panel:** High ionization state, $\log(\xi) = 1.5, 2$; black and red lines respectively. **Bottom panel:** Lower ionization state, $\log(\xi) = 0.5, 0.7, 0.9$; black, red and blue lines respectively. It can be observed that at higher $\log(\xi)$, the produced absorption feature is at bluer wavelengths.

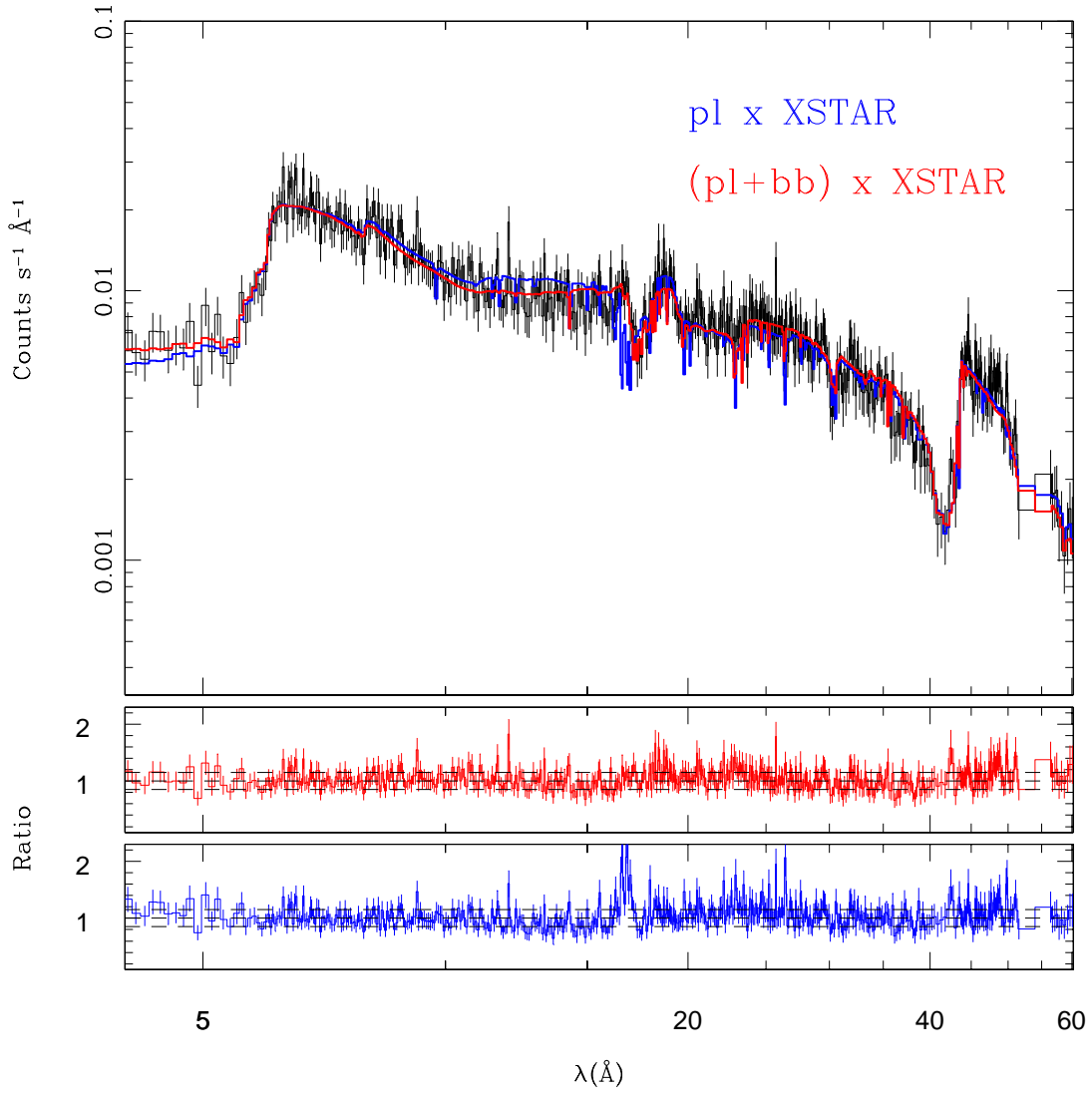


Fig. 7.— The best-fit XSTAR photoionization model (blue). A residual is seen at $\sim 17 \text{\AA}$. An important improvement is achieved by the inclusion of a thermal component (red). See Table 5 for parameter values.

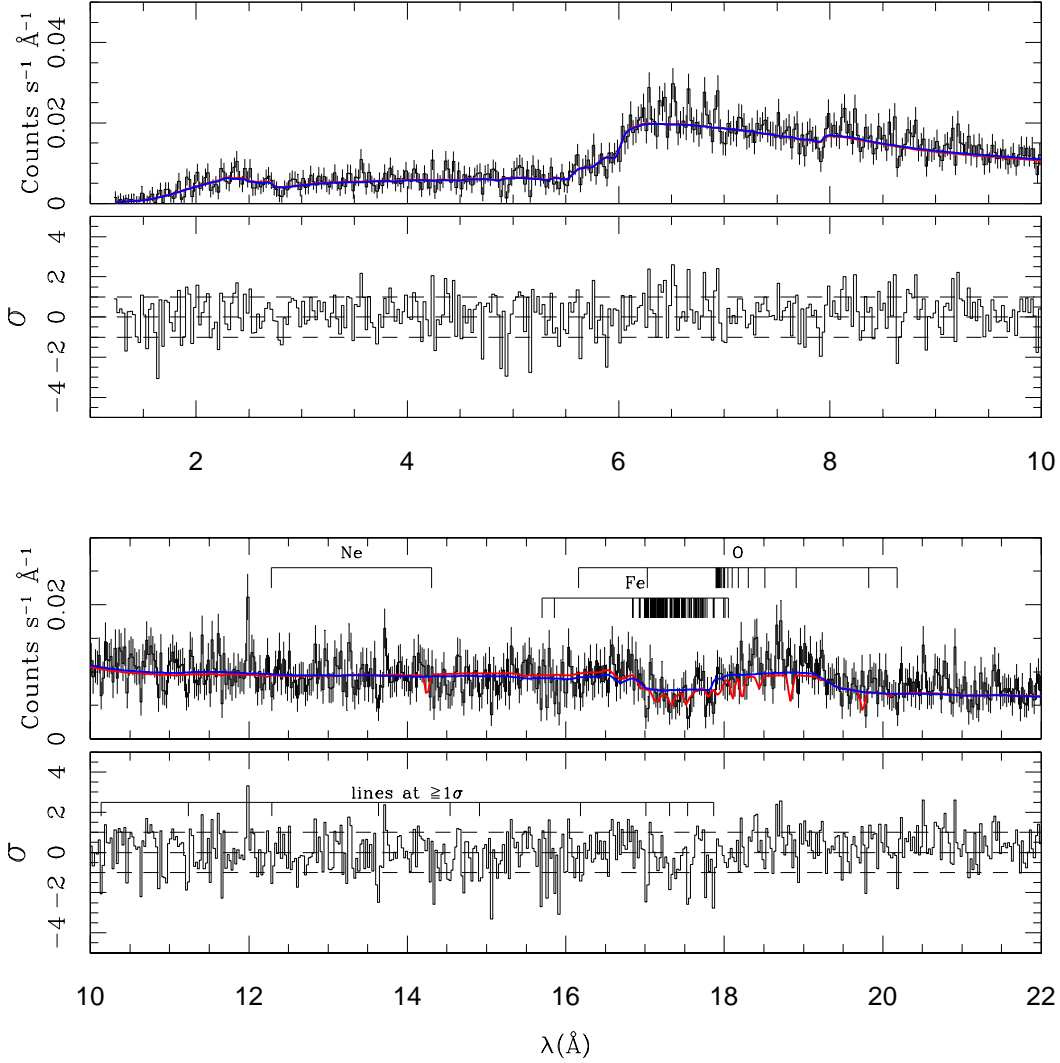


Fig. 8.— Comparison of the spectrum of MR 2251–178 with our best-fit XSTAR photoionization model which is presented in high resolution (bin size 25 mÅ). The physical model is shifted by -1100 km s^{-1} . Predicted lines of Ne, Fe, O, C and N are marked as labels in the top of the spectrum.

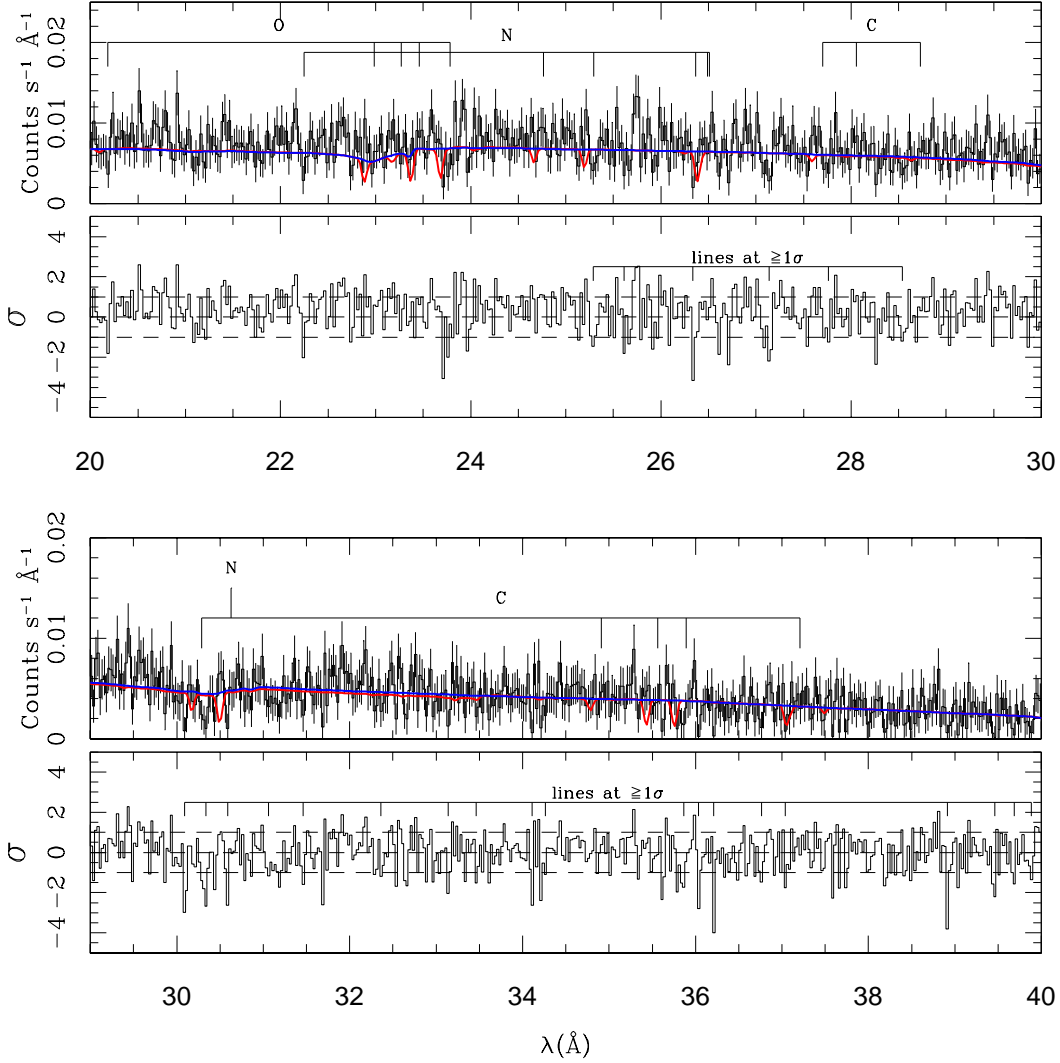


Fig. 9.— Comparison of the spectrum of MR 2251–178 with our best-fit XSTAR photoionization model which is presented in high resolution (bin size 25 mÅ). The physical model is shifted by -1100 km s^{-1} . Predicted lines of Ne, Fe, O, C and N are marked as labels in the top of the spectrum.

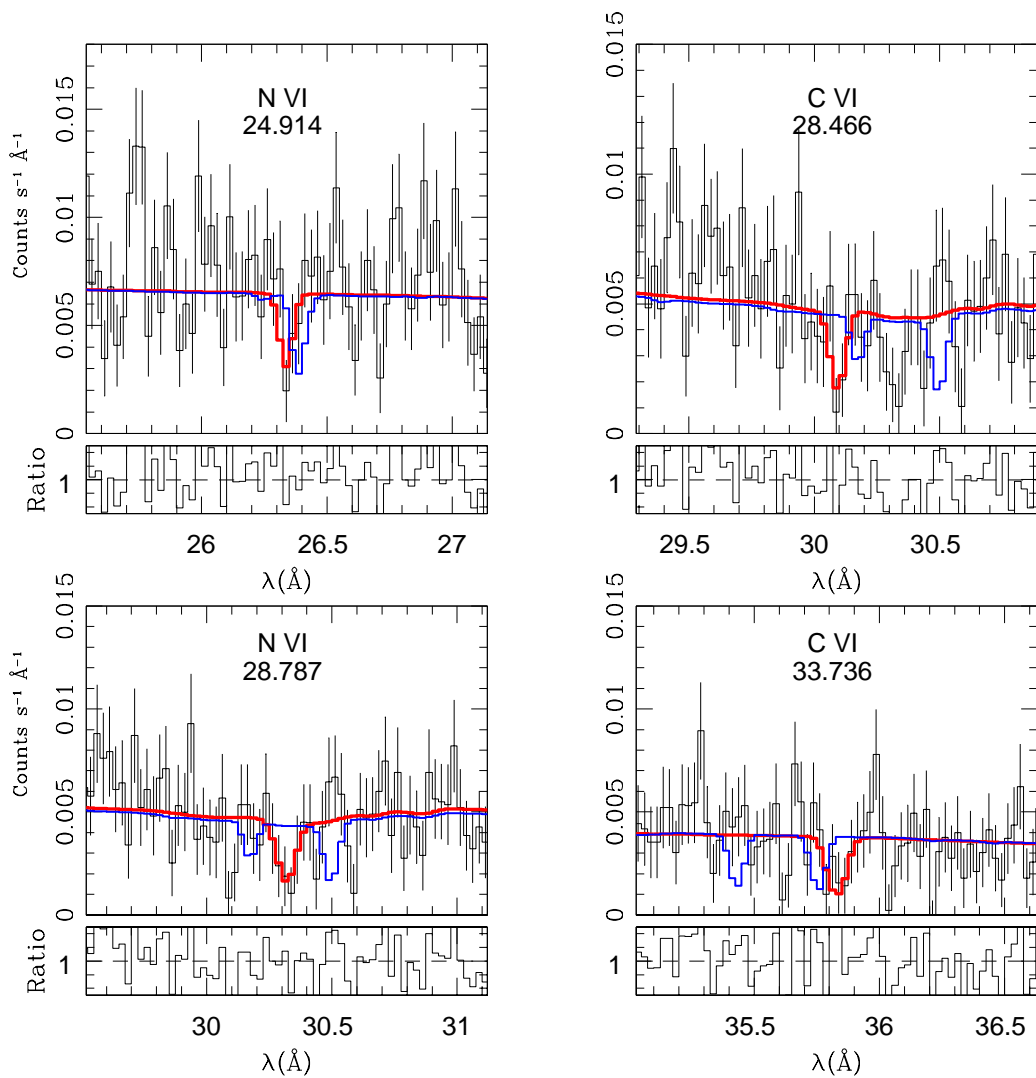


Fig. 10.— Strongest candidate absorption lines. The K_{α} and K_{β} lines of C VI and N VI show at least three outflow components at ~ -600 , -2000 and -3000 km s⁻¹. In red the Gaussian fit, in blue the XSTAR model shifted by -1100 km s⁻¹.

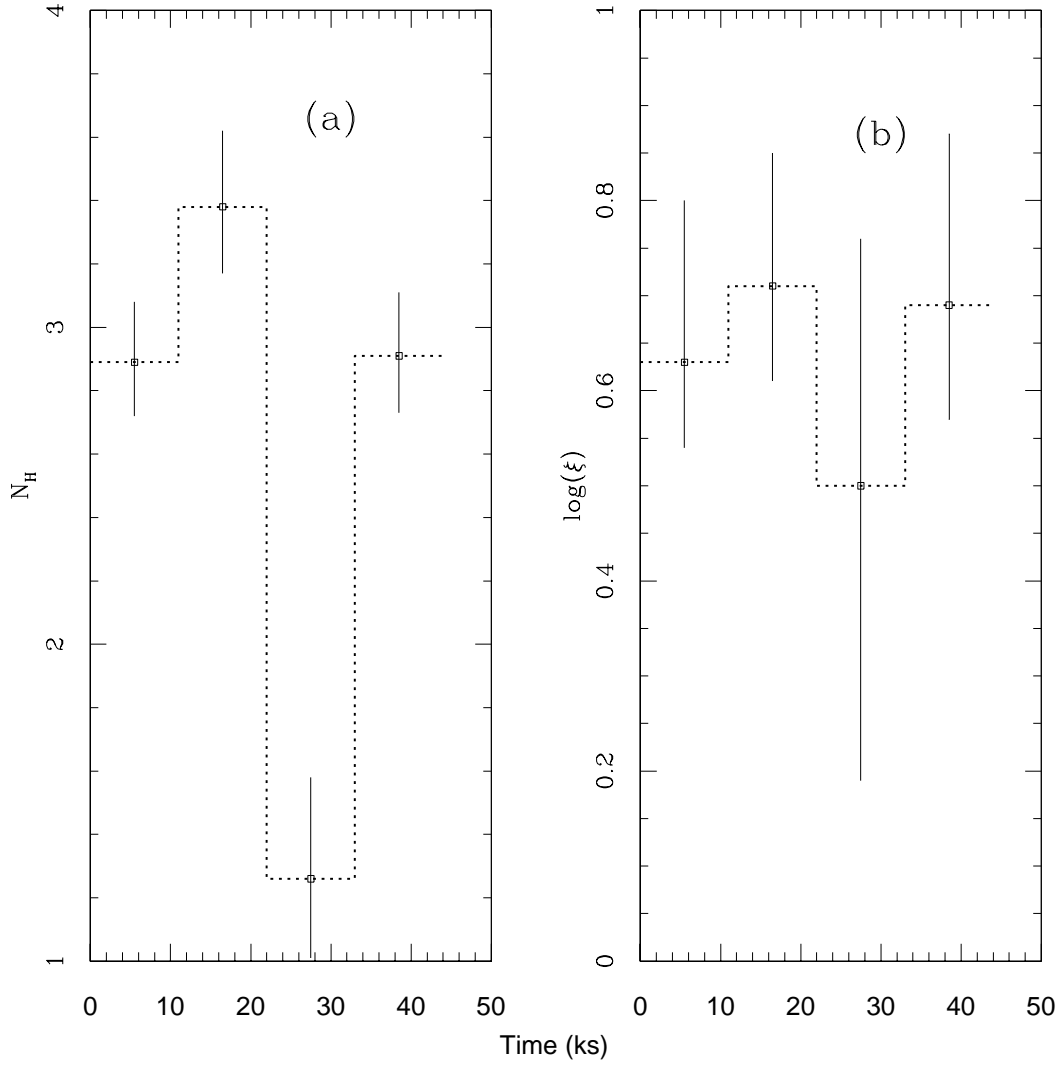


Fig. 11.— Time variability of the parameters for our model X_4 with the column density N_H of the warm absorber free to vary. (a) Column density in units of 10^{21} cm^{-2} . (b) Ionization parameter $\log(\xi)$, with ξ in units of erg cm s^{-1} .

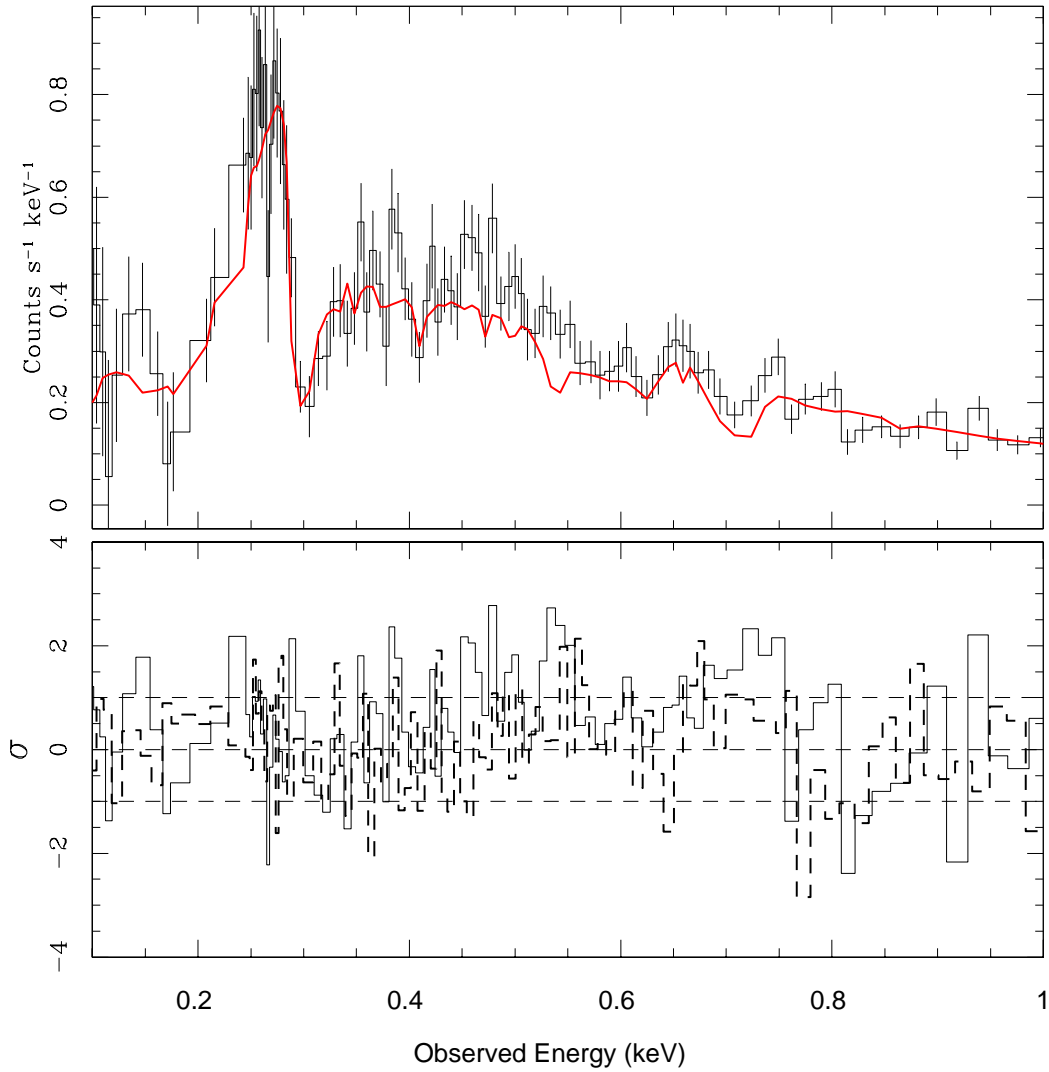


Fig. 12.— Best-fit model (X_4) resulting from epoch (1) with $\chi^2_\nu = 1.1$ (interrupted-line), applied to the data of epoch (3) (solid-line). Deviations are seen in the soft X-ray band ($\chi^2_\nu = 1.7$).